Design & Fabrication of Superconducting Josephson Devices for Quantum Measurements

Acknowledgments

This work would have been impossible without help and cooporation of many. I would like to thank those who helped and contributed to this research, and those who helped me create and develop it. First of all I would like to thank my supervisor, Nadav Katz, whom except for meaningful guidance kept encouraging me to develop personal thinking and creativity. I thank the lab staff, Yoni Shalibo, David Shwa, Roi Resh and Raffi Cohen, who was an active partner either by new ideas and directions, or by helping me whenever I needed. I would like to thank also Avraham Klein and Dr. Anayesu Melisa, who helped me at the beginning of the research and enabled me a quick entrance. As part of my research I was asked to form special electric circles which demand special conditions and equipment and therefore I had to use the 'clean room'. This is where I would like to thank the fabrication team of the Nano Center in the Hebrew University, headed by Dr. Shimon Eliav, who helped at all times and were involved in the solution to every problem I faced. I would like to end with special thanks to my dear wife, who supported and encouraged me along the way, and my three wonderful daughters- Dolev, Ya'ara and Shachar.

Abstract

In recent years, there has been growing interest in quantum computation. Most of the research focuses on building a quantum computer and on the use of controlled quantum systems for testing fundamental quantum theory. There are many physical systems which be used as controlled two-level systems (qubits). In our lab we use a superconducting device which has a unique element called a 'Josephson junction'. This element can be described as a non-linear inductor, a feature which allows the circuit to be used as qubit. Superconducting qubit devices are fabricated using the modern technology of lithography, deposition (oxidation) and etching. The fabrication must be carried out in a clean environment to avoid dust or any other kind of contamination that can damage the device.
Short dephasing times pose one of the main challenges in realizing a useful quantum information processing device. Different approaches have been devised to cure this problem for superconducting qubits. In this thesis we offer a new qubit design which should extend the coherence time of the phase qubit.
Our new circuit design is unique in that it contains a chain of Josephson junction in addition to the usual components. According to the behavior of the Josephson junction as a non-linear inductance, this chain functions as a large inductor (in the regime of weak drive current I, much smaller than the critical current of the junctions I_0). This large inductance reduces the influence of 1/f noise in the circuit. Using a simulation that calculates the effect of such a large inductance on the coherence time we designed a phase qubit with an enhanced coherence time.
To acquire the ability of qubit fabrication, we were required to successfully fabricate a single junction and to characterize our materials (Sapphire and Aluminum).

Besides the work on the special qubit design this thesis contains two other main projects that are not directly connected to qubits: shunt resonators and a theoretical project on quantum random walk
Chapter 3 summarizes our work with shunt resonators. At low temperatures, superconducting circuits have zero resistance, this allows them to have a very high quality factor. In our work we show an ability of fabricating and measuring of a quality factor of more than 100,000 at low power and more than 500,00 at high power. Moreover, we approach the single photons limit.
In chapter 5 we present a theoretical experiment on quantum random walk (QRW). Unlike

classical random walk, QRW has long range correlations in such way that we do not see the familiar Gaussian in the occupation probability. Our work presents a way to observe QRW of a single photon or a pair, in a system of superconducting coupled resonators.

Contents

Chapter 1

General Introduction

The general introduction focuses on the theory of the main device, the qubit. This chapter is composed of three main parts. I begin with a brief description of superconductivity phenomenon with emphasis on the Josephson Junction effect [1]. Next I introduce the Hamiltonian of the qubit and discuss different types of qubits [2, 3, 4] . Finally, I outline the materials and methods used for fabricating the devices.

1.1 Superconductivity and Josephson tunneling.

A microscopic theory explaining superconductivity has been formulated in 1957 by Bardeen, Cooper and Schrieffer (BCS theory). According to their theory, conduction electrons with opposite spin and momentum form a bound pair under the influence of a lattice phonon-induced attraction. The resulting particle, a so-called Cooper pair, has zero spin and hence obeys the Bose-Einstein statistics. This implies that, at low temperatures, all Cooper pairs condense into a ground state of lowest energy which can be described by a macroscopic wave function $\psi(r,t)$ (r being the spatial variable and t being the time).
$\Psi(\mathbf{r},t)$ can be written as $|\Psi(\mathbf{r},t)|\exp[i\delta(\mathbf{r},t)]$: that is, as the product of an amplitude and a factor involving the phase δ. Furthermore, in 'conventional' superconductors such as Nb, Pb and Al, the quasi-particles (electron-like and hole-like excitations) are separated in energy from the condensate by an energy gap $\Delta = 1.76\,k_B T_C$ (where k_B is the Boltzmann constant and T_C is the superconducting transition temperature). Thus, at temperatures $T \ll T_C$, the density of quasi-particles becomes exponentially small. In 1962 a British physicist named Brian David Josephson predicted mathematical relationships for current

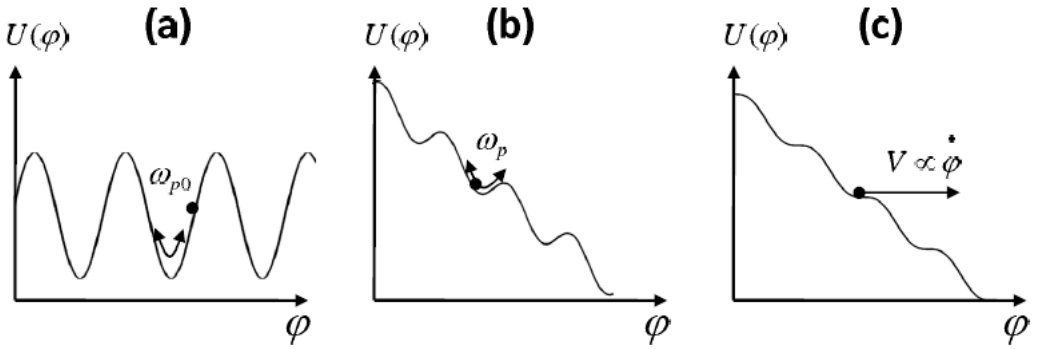

Figure 1.1: Effective potential of the current bias with (a) no bias (b) bias lower than the critical current (c) bias equal to the critical current.

and voltage across two superconducting layers separated by a thin insulating barrier:

$$I = I_0 sin(\varphi) \tag{1.1}$$

Here φ is the superconducting phase difference across the junction and I_0 defines the critical current of the junction, which represents the maximum super-current allowed by the junction. I_0 depends on the barrier thickness and the junction area. The second Josephson equation relates the time evolution of the phase difference φ to the voltage V across the junction.

$$\frac{d\varphi}{dt} = \frac{\Phi_0}{2\pi} V \tag{1.2}$$

where $\Phi_0 = \frac{h}{2e}$ is the quantum flux, e is the electron charge and h is Planck's constant. In contrast to a linear inductor for which $\frac{dI}{dt} L = V$ using equations 1.11.2 we can define the inductance of the junction as $L_j = \frac{\Phi_0}{2\pi\left(I_0^2 - I^2\right)^{\frac{1}{2}}}$. In addition, every Josephson junction has a finite capacitance in parallel to its inductance. Thus at small current bias ($I \ll I_0$) it behaves like a harmonic oscillator having a resonance frequency $\omega_{p0} = \frac{1}{\sqrt{L_{j-linear} C}}$ called the plasma frequency, where $L_{j-linear} = \frac{\Phi_0}{2\pi I_0}$ is its inductance at zero current bias. In the case of a finite or zero current bias, the resonance frequencies are current dependent and the oscillator becomes an anharmonic oscillator. The Hamiltonian of a current-biased Josephson junction is given by: $H = 4E_c N^2 - E_j cos(\varphi) - \frac{\Phi_0}{2\pi} I\varphi$ where N is the number of particles on the junction capacitance, $E_j \equiv \frac{\hbar}{2eI_c}$ is the Josephson energy and $E_c \equiv \frac{2e^2}{C}$ is the charging energy [3]. The dependence of the effective potential on the current bias is

shown in Figure 1.1.

1.2 Types of Qubit circuits

The second quantization of the electrical circuit defines the phase difference on the junction, φ, and the charge on the capacitor Q ($Q = -2eN$) as the relevant operators in our system, (similar to X and P in a classical harmonic oscillator) [2]. As conjugate operators they maintain Heisenberg's uncertainty principle. It follows that when φ is well defined Q has large quantum fluctuations and when Q is well defined φ has a large quantum fluctuations. In other words we can say that E_J/E_C (defined above) determines which of the variables is well defined. The demand for reduced sensitivity to noise has led over the years to three main qubits types: flux, phase and charge. Flux and phase qubits have a large ratio of E_j/E_c. In these systems the phase is well defined and thus the charge has large quantum fluctuations. As a result both these systems are less sensitive to charge fluctuations. In addition, the flux qubit has the advantage of being insensitive to first order fluctuations in flux, while the phase qubit has the advantage of being more tunable [5, 4]. The charge qubit operates in the opposite limit ($E_j/E_c \ll 1$) which reduces the sensitivity to current fluctuations. Different approaches have been devised over the last 5 years in order to cure the problem of short coherence time. Examples for this are the Transmon [6], the 3D Transmon [7] and the Fluxonium [8]. The Transmon is similar to the charge qubit in that both of them contain Cooper pair box, however, unlike the charge qubit, the Transmon was designed to operate in a regime of significantly increased ratio of Josephson energy and charging energy E_j/E_c (close to 10). This unique design reduces charge noise using the exponential sensitivity of energy level to E_j/E_c. The 3D Transmon is a Transmon qubit which is placed inside a macroscopic cavity (replacing the microscopic cavity that was used before). This reduces the coupling to undesired cavity modes. Moreover, this cavity can be designed in such a way that the charge fluctuation is reduced. Still, the 3D Transmon has a 'new' problem; it has a weak coupling to the environment. The Fluxsonium is a charge qubit that use an array of junctions to get a charge qubit free of charge offset, in this way it reduced the charge fluctuations.

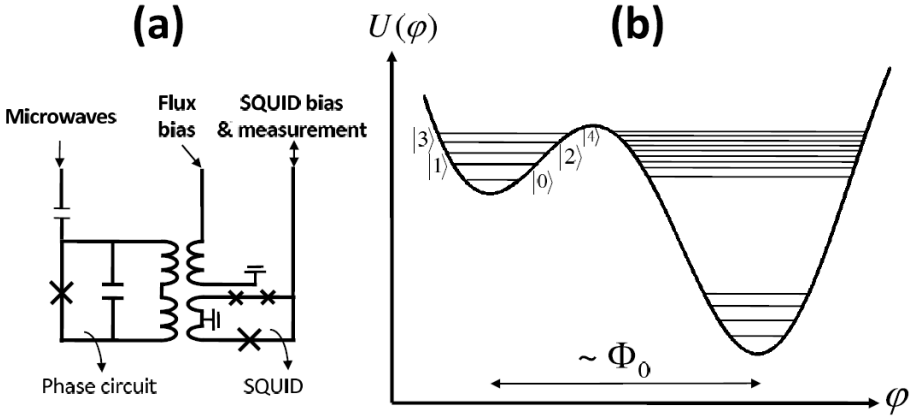

Figure 1.2: The flux-bias phase circuit. (a) circuit schematics (b) effective potential with energy levels

1.3 The flux-biased phase circuit

Unlike the current bias, where the current source is connected directly to the circuit, in the flux biased system the current is transformed by flux (Figure 1.2 (a)). The Hamiltonian for such a circuit with a flux bias $\Phi_{ext}$and a loop inductance L is:

$$\mathcal{H} = \frac{8e^2N^2}{C} - \frac{I_0\Phi_0}{2\pi}cos(\varphi) + \frac{1}{2L}\left(\Phi_{ext} - \frac{\varphi\Phi_0}{2\pi}\right)^2 \tag{1.3}$$

The potential of this Hamilonian is plotted in figure 1.2 (b). By tweaking Φ_{ext} we control the number of states in the well. This also affects the linearity of system, which is defined as the energy ratio of the second and first energy transitions (in a linear harmonic oscillator all energy transitions are equal). The state of this circuit is controlled by introducing microwave currents into the circuit, either directly or by applying a secondary flux. The microwave signals (typically between 5 to 15 GHz) are resonant with the qubit transition and thus can be used to create arbitrary superpositions of states. The state is measured by applying a short flux bias pulse that adiabatically lowers the potential barrier down to a point where the upper level is preferentially tunneled out of the well. Because of the fundamental relation between the phase difference across the junction and the total flux through the loop, the phase can be measured later by an on-chip superconducting quantum interference device (SQUID).

1.4 Design and fabrication of quantum circuits.

Quantum circuits are typically printed on sapphire or silicon wafers using optical or electron-beam lithography and thin film deposition. They present themselves as a set of micron-size or sub-micron-size circuit elements (Josephson junctions, capacitors and inductors) connected by wires or transmission lines. The electrodynamics of the circuit can be analyzed using simple transmission line equations or even a lumped element approximation. Contact to the chip is made by wires bonded to mm-size metallic pads. The circuit can be designed using conventional layout and classical simulation programs. Because of the sensitivity to dust and other particles, the fabrication process is carried out in a clean room.

Chapter 2

The Josephson Junction

2.1 Introduction

The Josephson junction is the main element in the qubit. Unlike the other elements that contain one layer, this element is composed of three layers, making its fabrication more difficult. A junction is defined by two parameters, the density of critical current (J_0) and its area. The product of these gives the critical current (I_c) of the junction. While the area is easily controlled by changing the design, the density of the critical current is much harder to set. The value of J_0 is determined by the thickness of the oxidation layer (isolated layer). The thickness of the oxidation layer is controlled by changing the time and pressure at the oxidation step, where the dependence of the thickness on the time behaves like $\sqrt{pt}$ [9]. At room temperature the relationship between the resistance and the critical current of the junction is described by the Ambegaokar-Baratoff formula [1]:

$$I_0 = \frac{\pi\Delta}{2eR} \tag{2.1}$$

where I_0 is the critical current , Δ is the superconducting gap, e is the electron charge and R is the resistance.

Serial Number	Area (μ^2)
1,10	0.5
6,7	1
2,11	2
8,9	4
3,12	8
4,13	16
5,15	32

Table 2.1: The area of junctions listed by their serial number

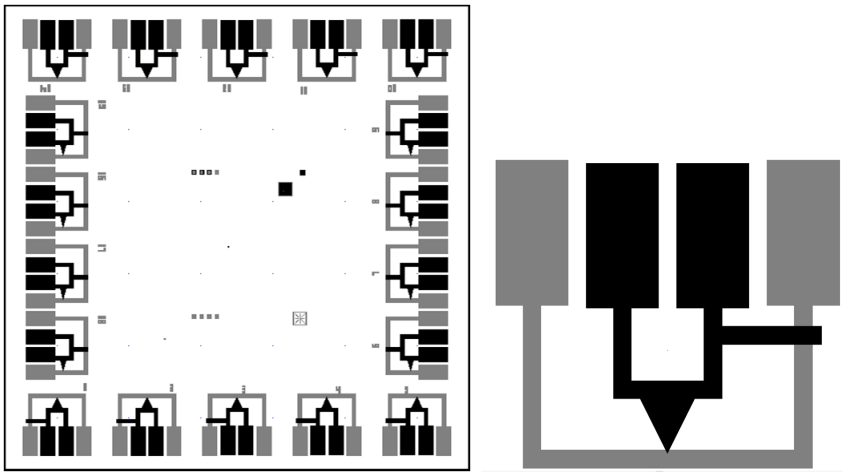

Figure 2.1: (Left) The 6.25 mm^2 designed chip, contains 18 junctions. The gray layer is the base layer and the black layer is the so-called junctions layer. (Right) A zoom-in on a single junction.

2.2 Experimental Design

2.2.1 4-Wires Measurements

Since the junction resistance is fairly small and the contacts between probes touching the wafer have a comparable or even larger resistance, it is necessary to employ a technique called a 4-wire measurement to measure the junction resistance independently of the lead resistance. For this, the junction is biased by a current through one pair of pads as shown in Figure 2.2. The voltage developed across the junction is then measured via the other two pads. Since the current can be determined reliably despite additional series resistance and since the lead resistance is negligible compared to the internal resistance of the volt meter, this measurement gives an accurate reading even under varying lead resistance. It

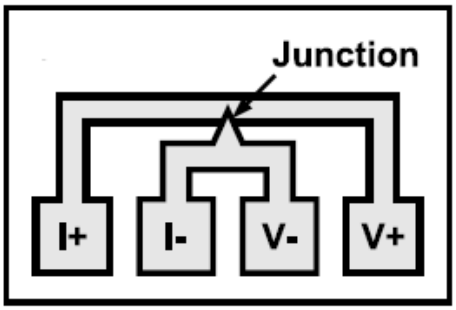

Figure 2.2: 4-Wires measurement : Each side of the junction to be measured is connected to two pads, one of which is used for a current bias and the other for a voltage measurement [10].

is very important to note that when we measure the junctions we do not generate high voltage on the junctions. During the measurement current flows in the junction, and so according to Ohm's law we get that the higher the resistance the higher the voltage on the junction. In order to avoid this problem we inject current as weak as possible. A direct result of this "problem" is the need to be extra careful with small area junctions.

2.3 Mask design

The geometry of the junction is quite straightforward and does not require many parameters. It contains two wires which have a small overlap (the junction) and four pads, one at each wire end. In our design, each pad was chosen to be $200 \times 400\mu^2$ to allow easy access during the measurement. We designed a $6.25 \times 6.25mm^2$ chip with 18 junctions of various areas (Table 2.1)(Figure 2.1) .The specific discussion on the characteristics and goals of each layer are found in appendix –.

2.4 Fabrication

The specific fabrication process, including the parameters that we used, will be described in appendix A, in this section there will be an overview of the process without the details. The fabrication process begins with the design of the layout in a standard graphic design program such as L-Edit. The design is exported to GDS files, which will be used for the lithography. Before starting the elaborate explanation, I will examine briefly the entire process starting from a clear wafer through the entire junction creation. (Figure 2.3).

At first we deposit the material on the wafer, then using lithography we get the desired pattern made of photo-resist on the wafer, after etching we get the so-called Base Layer. The next step is creating the 'isolator' layer (aluminum oxide). On the 'isolator' layer we deposit another aluminum layer that is etched carefully after another lithography process then the junction is done (in our specific case there is still need for wet etch as written above).

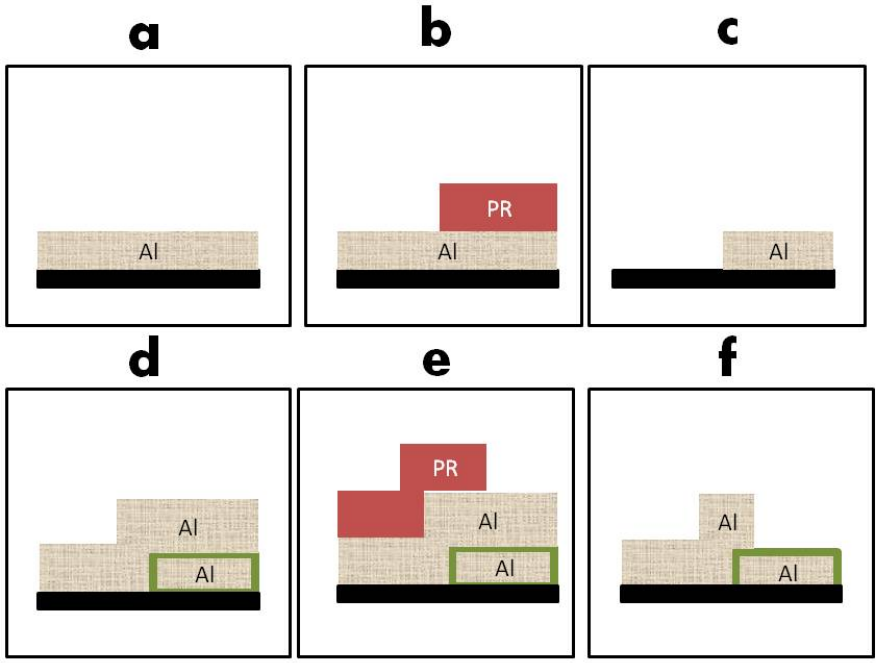

Figure 2.3: The fabrication process of Josephson Junction: (a) Deposition of a thin film of Al on the wafer. (b) First lithography, creates the 'base layer' made by photo-resist. (c) After first etch, 'base layer' made by Al. (d) Oxidation the first layer and deposit second Al layer. (e) Second lithography step, creates the 'junction layer' . (f) After second etch the junction received.

2.4.1 Deposition & Oxidation

We work with wafers of silicon or sapphire. The advantage of sapphire is small losses, silicon on the other hand is much cheaper, therefore the qubits and the resonators were made with sapphire while for the junctions we use silicon. Once we chose the substrate, we deposit thin film of aluminum (around 200 nm). This deposition is done using a method

called 'Sputtering'. Sputtering is a process in which a disc of pure aluminum ('the target') is bombarded with argon ions. The impact causes aluminum atoms to be ejected from the target. If the wafer is positioned close to the target, some of the ejected aluminum atoms will hit and stick to the wafer. The rate at which this layer grows is slow enough to allow for its thickness to be controlled to an accuracy of several nm. Sputtering is done in a vacuum system to remove contaminants. The oxidation process is also done in the sputtering machine by exposing the wafer to oxygen, after ion milling and before depositing the second layer.

2.4.2 Lithography

The blanket aluminum film now needs to be defined into the traces required for the base wiring layer. This is done via an RIE (see section 2.3.3) through a mask of photo-resist. The mask is created in a process called photo-lithography. For this, the entire wafer is covered with a photo-resist, a polymer-solution that changes its solubility when exposed to UV light. The covered wafer is exposed to UV using machine called 'Mask Aligner'. The Mask Aligner exposes the wafer to 386nm UV. A chrome mask that carries the desired pattern, is between the UV and the wafer, functioning as a UV filter. The result of this exposure is a photo-resist mask on the wafer that carried the patter that we want. The second lithography is performed in the same way. Another way to create the photo-resist mask is to use a 'direct write' method (the same method that was used to create the chrome mask). This method contain a laser beam which 'writes' the desired pattern on the photo-resist. This writing is equivalent to the exposure in the 'Mask Aligner'.

2.4.3 Dry Etch

After the lithography process the wafer is loaded into a machine called RIE (Reactive Ion Etching). This machine works by creating a plasma of reactive gases, which etches the required material via chemical reaction. In our case when the material is Al, the chamber is filled with a low pressure of mixture of Ar and HBr providing slow chemical etching ($\sim 100\frac{nm}{min}$). Since the etching is done slowly it allows us to control it, a feature which is very important to us. After the unwanted aluminum vanishes, the residue of the photo-resist is removed using ion milling. This step should be delicate in the second etching, to avoid keeping a residue of aluminum from the top layer on one hand, and refrain from etching down to the sapphire and damaging the 'base layer' on the other hand. One way

we tried to avoid this problem was to check the wafer every 30 seconds, so in the worse case the base layer thickness would be 100-150 nm.

2.4.4 Wet etch

Unlike the dry etch, this step is insensitive. The wet etch is done using a mixture of H3PO4 (Phosphoric Acid), HNO3 (Nitric Acid) and Acetic Acid that are heated to fifty degrees.

2.5 Result & Discussions

Figure 2.4 shows an example for the junction's resistance that has been measured from a single chip (as written above any chip includes 18 junctions). It can be seen that the linear behavior is as expected, yet the graph shows a problem that exists in small area junctions. This could be explained by some problems in the fabrication process e.g. aggressive etching, rough sputtering .etc. The problems could be classified into two classes: problems that cause destruction of 'working' junction such as high current at the 4-wire measurement and problems that occur in the fabrication process thereby destroying the junction before it was even created. The main candidate for the second type of problems would be aggressive etching. Aggressive etching can cause a rough surface as can be seen in Figure 2.5 , plays a major role mainly in small area junctions.

By using Ambegaokar-Baratoff formula (Eq 2.1) when we take Δ to be $170\,\mu eV$ (the energy gap of aluminum) the critical current density (j) that matches the chip in figure 2.4 is $j \sim 1.3\frac{\mu A}{\mu^2}$. This means that a junction with an area of $1\,\mu m$has critical current of $1.3\mu A$. Our goal is around $j = 0.5\frac{\mu A}{\mu^2}$ so that a junction of one square micron will give $I_0 = 0.5\,\mu A$. Since even under the same conditions different wafers can have different critical current density this result is a good start.

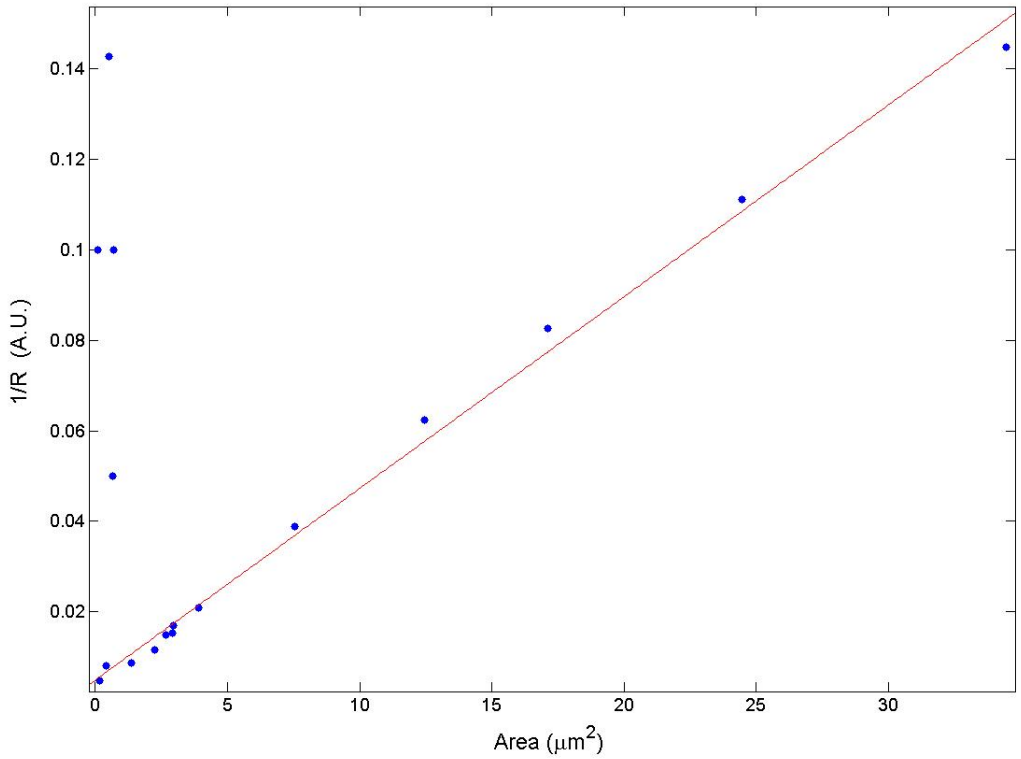

Figure 2.4: The inverse resistance as function of the junction's area: This chip has been done under oxidation parameters of P=20 mT for 5 min and it present density critical current of $j \sim 1.3\frac{\mu A}{\mu^2}$.

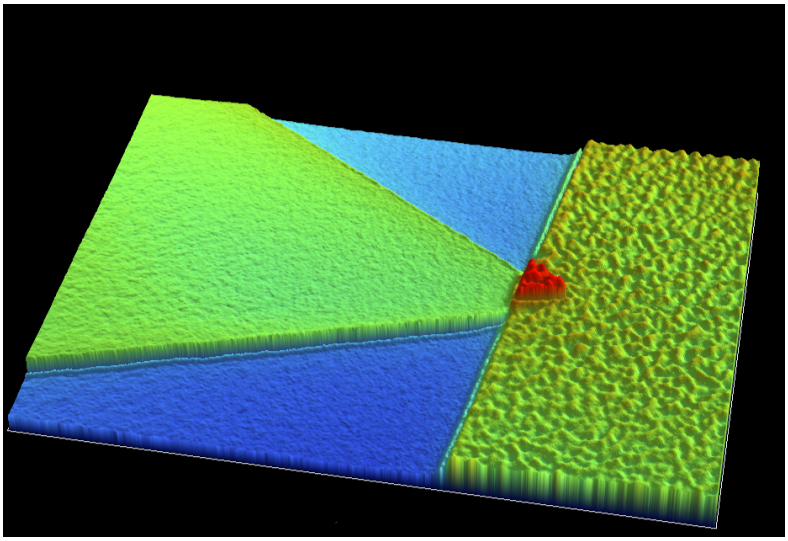

Figure 2.5: A picture of the junction taken via optical surface profiler. It can see clearly the different between a smooth surface (the triangle) and a rough surface. This kind of problem can be the reason of failed small junctions.

Chapter 3

The Superconducting Resonator

Up to this point we discussed the fabrication and characterization of Josephson junctions. This chapter will discuss a new element, a superconducting resonator, which is not directly related to the previous topic, but is another link in the development of a qubit.

3.1 Introduction

Superconducting transmission line resonators can be used to read out different sensors, e.g. flux qubit, transmission edge sensor .etc. For both applications, high loaded quality factors of the microwave resonators are required, so it is possible to detect small deviations in their resonance frequency. Superconducting resonators behave like harmonic oscillators, a feature that can be used to study quantum random walk (Chapter 5). This chapter will discuss our work on superconducting resonators. This work includes design, fabrication and characterization that are inspired by Mazin's thesis [11].

3.2 Resonator theory (Analytical analysis).

The Quarter wave transmission line resonator is simple conceptually, easy to build and couple, and its resonance is very easy to find. The resonant microwave circuits, such

as micro strip transmission lines, exhibit sharp resonances at distinct frequencies. In the vicinity of each resonance, the behavior of the resonator may be described by an equivalent lumped resonant circuit. The analytical analysis of superconducting transmission line resonators in this section follows the analysis found in Mazin's thesis[11].

The measured Q of a resonator is expected to depend on the total energy loss per cycle of the resonator. We expect energy to leak out through several paths. Some paths, like the one through the coupling capacitor, can be controlled by the design, while others, like the loss of energy to electromagnetic radiation, are governed by geometry and material parameters. These loss terms add like resistors in parallel:

$$\frac{1}{Q} = \frac{1}{Q_{Coupling}} + \frac{1}{Q_{Radiation}} + \frac{1}{Q_{Dielectric}} \tag{3.1}$$

where Q is the measured quality factor, and the other terms represent the energy that leaks out of the resonator at the coupling capacitor, dielectric loss and radiation loss. If all other loss terms are negligible compared to Q_c (coupling Q), then the measured Q of the resonator will be close to Q_c. The losses to the dielectric material and from radiation will be discussed extensively in 3.2.2.

3.2.1 Quarter wave transmission line resonator

The quarter wave transmission line resonator, shown in figure 3.1, consists of a series combination of a coupling capacitor C and quarter wavelength section of transmission line of impedance Z_0, shunting a feed line. Here we follow the analysis of Day as it appear in Mazin's thesis [11]. The input impedance, Z_l, of the shorted transmission line is:

$$Z_l = Z_0 tanh\left(i\beta l + \frac{\beta l}{2Q_i}\right) \tag{3.2}$$

, where β is the propagation constant, $Q_i = \beta/2\alpha$ is the internal quality factor of the line, and α is the attenuation constant. Near the quarter-wave condition, we can write

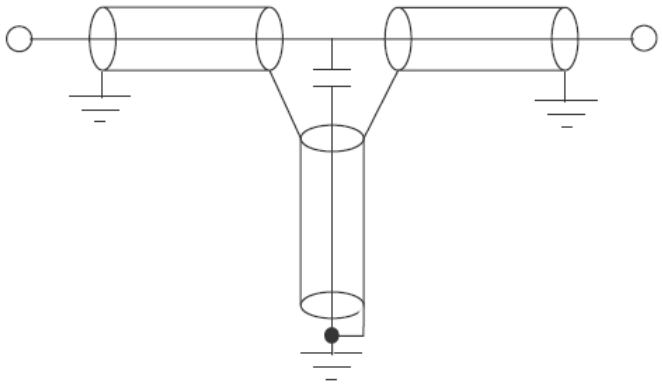

Figure 3.1: A quarter wave transmission line resonator shown represented schematically with coaxial transmission lines.

$\beta l = \frac{\pi}{2}\left(1 + \frac{\omega - \omega_{1/4}}{\omega_{1/4}}\right)$,where $\omega_{1/4}$ is the angular frequency when the quarter wave condition is met. Dropping second order terms of $\frac{\omega - \omega_{1/4}}{\omega_{1/4}}$ given us the final expression for Z_l:

$$Z_l \approx \frac{4 Z_0 Q_i}{\pi\left(1 + 2iQ_i \frac{\Delta\omega}{\omega_{1/4}}\right)} \tag{3.3}$$

where $\Delta\omega = \omega - \omega_{1/4}$. Calculating now the total impedance of the circuit and using the forward scattering matrix element for a shunt impedance

$$S_{21} = \frac{2}{2 + \frac{Z}{Z_0}} \tag{3.4}$$

give us the expression:

$$\left|S_{21}^{min}\right| = \frac{Q_c}{Q_i + Q_c} \tag{3.5}$$

Near the resonance the resonance curve can be expressed as:

$$S_{21} = \frac{S_{21}^{min} + 2iQ\delta x}{1 + 2iQ\delta x} \tag{3.6}$$

where Q is the measured quality factor. Under the assumption that the energy leak coming from dielectric loss and radiation loss can be neglected $Q = Q_i Q_c/(Q_i + Q_c)$ at $T = 0$.

3.2.2 Losses

Leaks from the capacitor - The expression that determines the amount of power that leaks out through the coupling capacitor is [11] :

$$Q_c = \frac{n\pi}{2Z_0 Z_l(\omega_n C)^2} \tag{3.7}$$

Typical values are: $C = 1\,ff$, $\omega_n \simeq 35\,GHz$ and $Z_0, Z_l = 50\Omega$ thus parameters gave $Q_c \sim 500,000$

Radiation Loss - The radiation loss for straight quarter wave resonator with semi-infinite dielectric, for the first mode based the analytically calculated that done by Vayonakis is[12]:

$$Q_{rad} = \frac{\pi(1+\varepsilon)^2}{2\varepsilon^{5/2}} \frac{\eta_0}{Z_0}(\frac{L}{S})\frac{2}{I'(\varepsilon)} \tag{3.8}$$

where ε ,($\varepsilon = 10$), is substrate dielectric constant,η_0 is the impedance of the free space, Z_0 is characteristic impedance of the line, L is the length of the resonator ,s is the width of the center strip plus the gap width and I'(ε) for a quarter wavelength is 0.33 ($\varepsilon = 10$). For a 6 GHz resonator the $Q_{rad} \approx 6 \cdot 10^6$.

Dielectric loss - $Q_{dielectric}$ is determined by the value of the loss tangent constant - $tan(\alpha)$ following the equation $Q_{dielectric} = \frac{1}{tan(\alpha)}$. Since we want to get α as small as possible we use a sapphire that has $\alpha \approx 10^{-7}$as the substrate.

3.2.3 Number of Photons

The 1/e decay time for the stored energy following the definition of the quality factor is:

$$T_1 = \frac{Q}{2\pi\omega} \tag{3.9}$$

From this relation we get an expression for the number of photons that occupy the resonator at resonance:

$$\langle N \rangle_{photons} = \frac{T_1 \cdot P_{res}}{\hbar\omega} \tag{3.10}$$

where $P_{res}$is the power inside the resonator at resonance (its equal to $\left|S_{12}^{off-resonance}\right|^2 - \left|S_{12}^{in-resonance}\right|^2$ multiply by the drive power) and $\hbar\omega$ is the energy of a single photon. Another phenomenon related to the power, is a dependence of the quality factor on the power. Beyond the energy loss mentioned above there are losses that comes from some defects in the substrate such as TLS (two level system) [13]. At high powers these TLS are saturated so that the Q factor is higher, however at low powers the Q factor decreases to a limit that depends on the substrate.

3.2.4 Mask Design

Unlike Josephson junctions and qubits, resonators have one layer. This fact makes their fabrication process much easier. The design includes three main parts: two pads (for readout signal), a feed line and ten resonators which are coupled to the feed line (figure 3.2). These resonators are researched extensively [14, 15, 16].

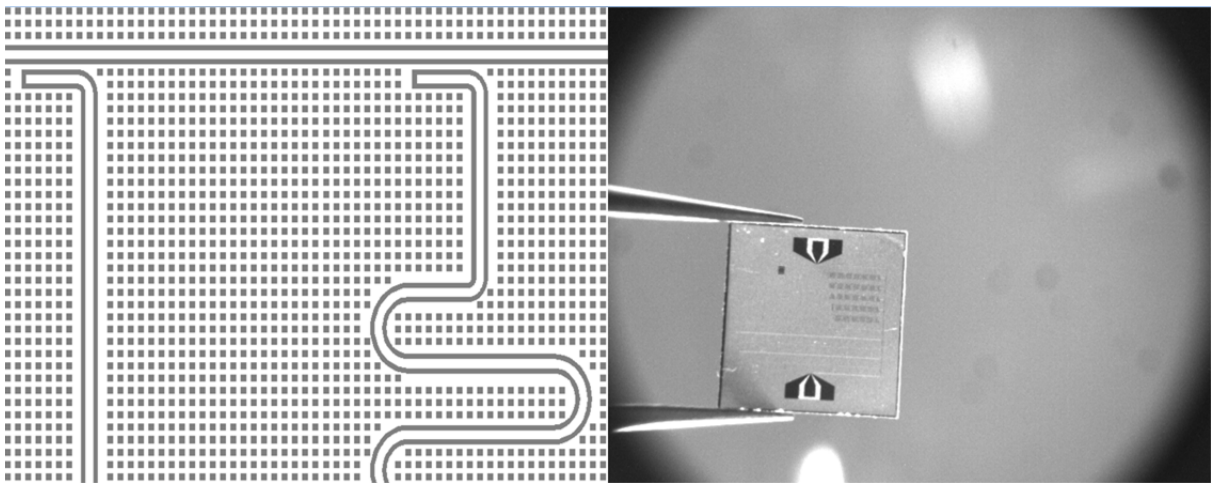

Figure 3.2: (Left) A part from the design as it shows in L-Edit. (Right) A 6.25 mm resonator chip.

3.2.4.1 Parameters Selection

Resonator length - The desired resonant frequency f_0 of the first resonance in conjunction with the dielectric constant sets the overall length of the resonator if there is no kinetic inductance present. A wave propagating on a loss-less transmission line with a vacuum dielectric will move at the speed of light. However, the addition of a dielectric slows down the propagation of the signal to a fraction of the speed in vacuum. This reduced speed, the phase velocity $\bar{c}$, can be calculated as

$$\bar{c} = c\sqrt{\frac{2}{1+\epsilon}} \tag{3.11}$$

where ϵ is the dielectric constant of the substrate and c is the speed of light in vacuum. In a quarter wave resonator the length of the transmission line l is $1/4$ of the wavelength. The length of a quarter wave resonator works out to be:

$$l = \frac{c}{4f_0}\sqrt{\frac{2}{1+\epsilon}} \tag{3.12}$$

Our design contains two groups of resonators, five straight resonators in the range of 6-6.5 GHz and five meander resonators in the range of 4-5 GHz. According to equation 3.12 the straight resonators are found in the range of 5-5.5 mm and the meanders in 6.5-8 mm.

Capacitor length - In order to couple the resonator to a feed line without breaking the ground plane we designed an "elbow coupler" as shown in Figure 3.2. Due to decisive influence of these parameters on the Q-factor and in order to get capacitance of around 1ff we ran a simulation in FastCap (where the parameter was the capacitor's length). The simulation gave us estimated value for a capacitor length of 50μ. As written above our mask contains five chips, which allow us to design each one with a different capacitor length (25, 50, 100, 150, 200 microns), hopefully in the range of 0.1-5 ff .

Coplanar wave guide geometry - The transmission line impedance of radio frequency electronics is usually 50Ω . This, in conjunction with the dielectric constant of the substrate, sets the ratio of the center strip width to the separation of the ground planes. The impedance can be solved for analytically, following Pozar book [17]for a semi-infinite dielectric:

$$Z_0 = \frac{30\pi}{\sqrt{(1+\epsilon)/2}} \cdot \frac{K(k_0')}{K(k_0)} \tag{3.13}$$

$$k_0 = \frac{s}{s+2w} \tag{3.14}$$

$$k_0' = \sqrt{1 - k_0^2} \tag{3.15}$$

where s is the width of the center strip, w is the width of the slots in the ground plane, and $\mathrm{K}(k_0)$ is the complete elliptic integral with modulus k_0 . This is important for the through line that runs past the resonator (the feed line). The CPW line of the actual resonator is decoupled from the feed line by its coupling capacitor so its impedance does not need to be 50Ω . In our case we take s and w of the feed line to be 8 and 3.8 respectively.

3.3 Experimental Design & Measurement

We can divide our experimental design into two parts, the first one is the cryogenic system (and all the wiring). The second part is the measurement system. script of the connection of the resonator in the fridge. picture of the holder.

3.3.1 Cryogenic system

The cryogenic system Oxford-Vericold dilution refrigerator, reaches a base temperature of 10 mill-Kelvins (mK). It contains several concentric height differentiated plates (as can be seen in Fig 3.3). Each plate has different temperature, the lower the plate the smaller and cooler it is. Cooling down to 10mK is done using He3/He4 mixture in a closed cycle. The plates are covered by three concentric Mu-metal cans screening magnetic fields.

Sample holder - As shown in Fig 3.3 the resonator lies at the center of the holder with two line of PCB connecting it to SMA connectors. The connection between the chip to the PCB is made via a wire bonder.

Wiring - Fig 3.3 describes the wiring inside and outside the fridge.

3.3.2 Measurement system

For signal generator and measurements we used NetWork Analyzer that has a frequencies spectrum of 2-20 GHz. All our measurements were of S_{12}(from S-matrix). In order to find the resonance frequency with a scan of $100MHz$ span, the signal must have high power (around -10 dBm). When the resonance is observed we start reducing the power, the span and the number of sampling points, until the circle in the S_{12} polar presentation shows completely. It is very important (for the fit) to take a lot of points from the edges besides

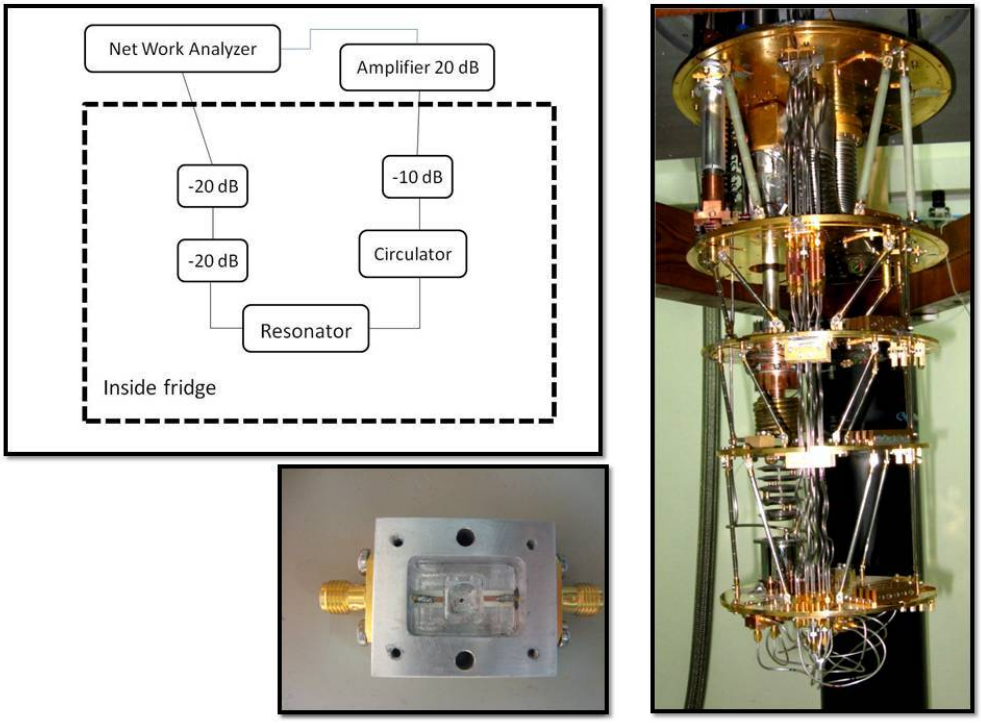

Figure 3.3: Left-Top - Description of the wires from the network analyzer (outside the fridge) to the resonator (inside the fridge). Left - bottom - The sample holder. Right - Oxford-Vericold dilution refrigerator without the Mu-metal covers.

Symbol	Description
Q	Resonator quality factor
f_0	Resonance frequency
a	Off resonance amplitude
v	Off resonance IQ velocity
c	Linear offset of the beginning and end of the resonance curve
θ	Rotation angle of the data with respect to the origin
g_I	Gain of the I channel
g_Q	Gain of the Q channel
I_c	Center of the resonance circle in the I direction
Q_C	Center of the resonance circle in the Q direction

Table 3.1: Parameters used to fit the resonance curve.

the points near the resonance already taken.
As stated above we are interested in the number of photons in the resonator at resonance. In order to get the number of photons, we need to know the absolute power on the resonator. Therefore we perform a measurement of S_{12} without the resonator (at room temperature) to get the total attenuation from the network analyzer to the resonator. The attenuation was found to be 50-55 dB, per line.
At the time of the measurement we saw the resonance as it shown in Fig to calculate the Q-factor and the the resonance we fit the result to an equation that contains shifting and bias in the phase and the amplitude.

3.4 Resonator Data Analysis & Discussion

Finding a resonance with a Q-factor of over 10,000 is not simple when we have about 8 resonances in a span of $3GHz$. by starting with $100MHz$ span in high resolution and than zooming in we succeeded in the finding.

3.4.1 Fitting resonator parameters

A resonance transmission curve in the complex plane can be fit with a robust nine parameter model that accounts for all the behavior observed in our resonance data. The parameters of the model are shown in Table 3.1 . The fitting function is evaluated in

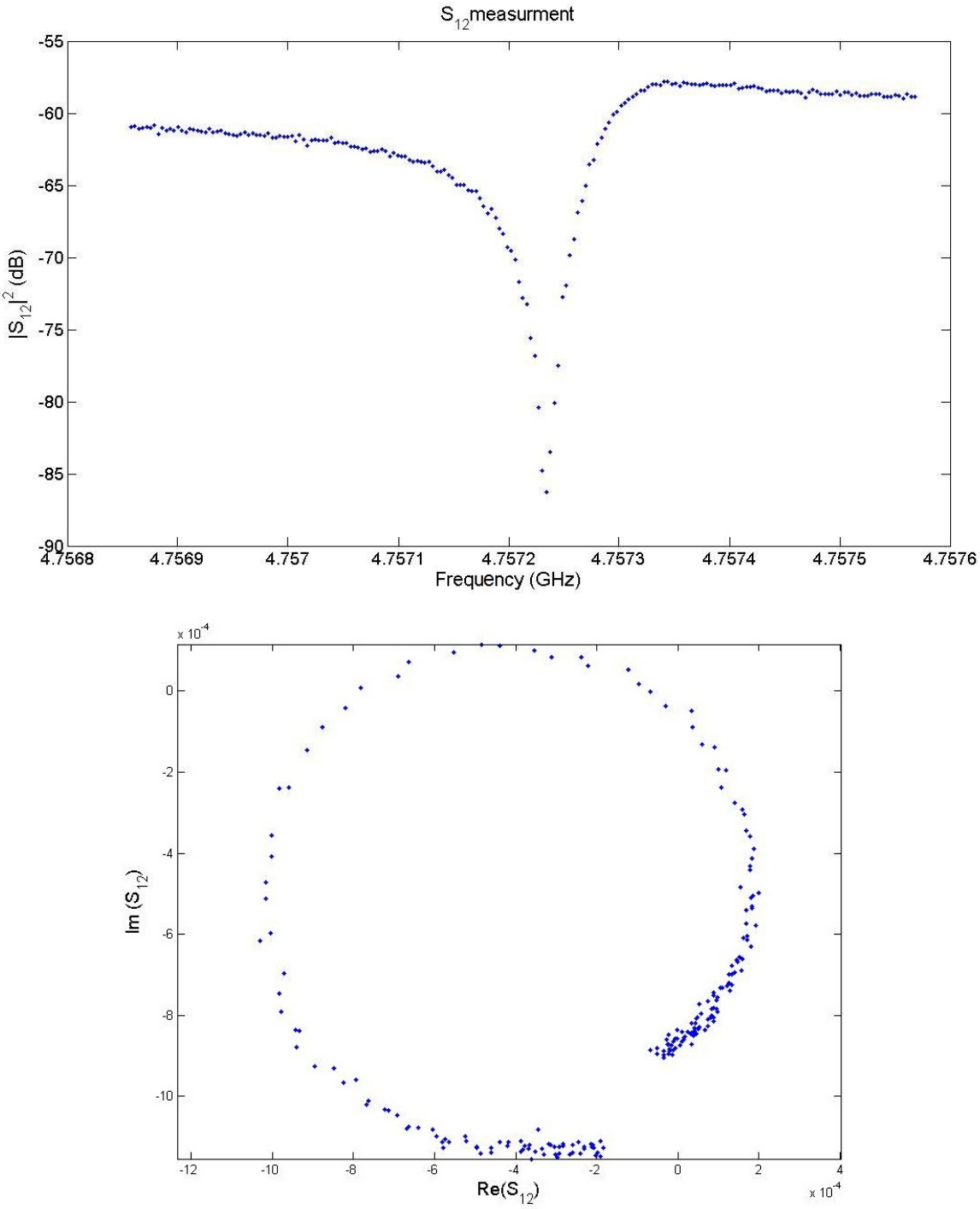

Figure 3.4: S_{12} measurement - This measurement was taken with -40 dBm power support, the suitable Q-factor is 40,000.

several steps for clarity.

$$dx = \frac{x - f_0}{f_0} \tag{3.16}$$

$$F = \frac{2iQdx}{1 + 2iQdx} - \frac{1}{2} + cdx + a(1 - exp(ivdx)) \tag{3.17}$$

The first term is derived from equation 3.6 and it describes a resonance feature centered at (0.5,0) in the complex plane, with the resonant frequency at (0,0) and the cross over of the resonance loop at (1,0). The second term is an offset to move the resonance feature in the complex plane, and the last two terms are leakage terms. This function must now be scaled, rotated by an angle , and offset to match the resonance data.

$$F_1 = g_I Re(F) + g_Q Im(F) \tag{3.18}$$

$$F_2 = F_1 exp(i\theta) \tag{3.19}$$

$$F_3 = F_2 + (I_c + iQ_c) \tag{3.20}$$

$F_3$is the final fitting function. To run the simulation we used Matlab with initial conditions (initial parameters) taken from a rough estimate of the data .

3.4.2 Data analysis

Table 2.1 shows the measured Q factor in a specific device, where the length of the coupling line was $50\,\mu m$. The first conclusion derived from looking at the results is that our devices support high Q , The coupling capacitor is the free parameter used to fit the measured Q to the designed Q. Figure 3.6 shows the measured Q and the designed Q. with different coupling capacitors, plotted on the same graph. The value of the coupling capacitor, as seen from the graph, is in the range of $0.5 - 1\,ff$. Comparison of the measured resonance frequencies to the designed resonance frequencies shows satisfactory results. As mentioned

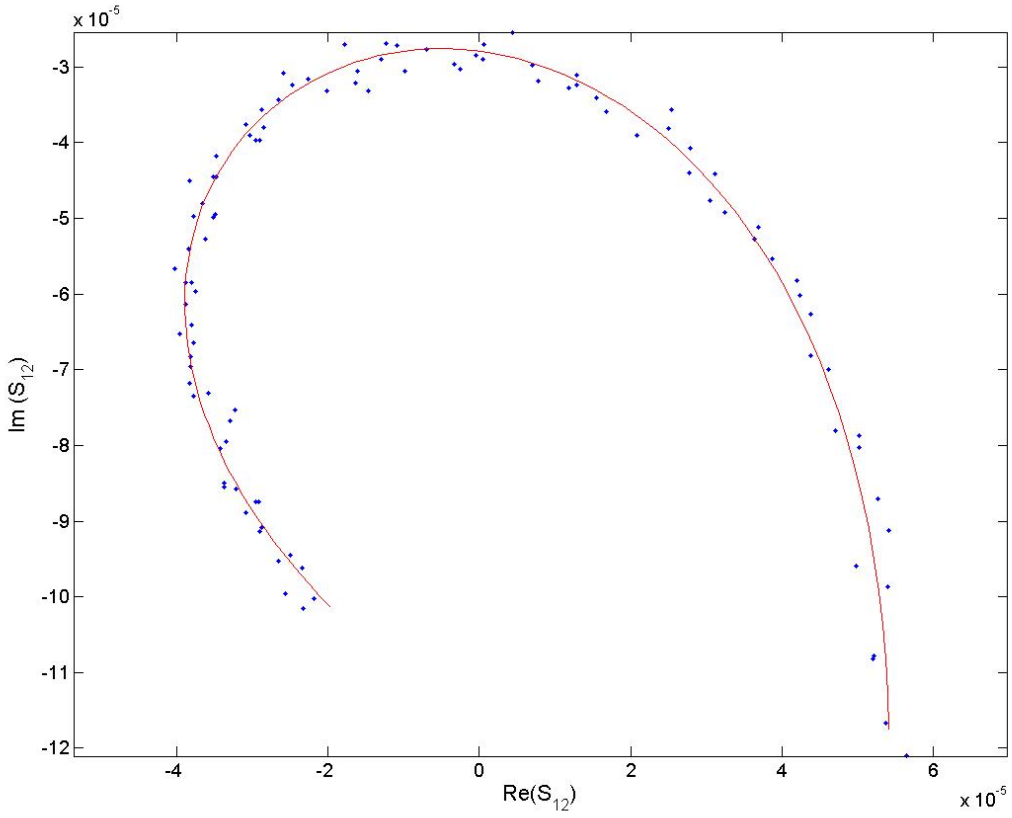

Figure 3.5: An example of the resonance fitting function's ability to match difficult resonator data. The blue points are actual measured data, and the red line is the result of a fit to the data.

above, our design contains five meandered resonators with resonance frequencies that are within the range of 4 to 5 GHz and five straight line resonators with resonance frequencies that are within the range of 6 to 6.5 GHz. Beyond the fact that only six resonances were measured (probably due to problems in fabrication process), it seems that the measured resonances and the gaps between the resonances were consistent with what was planned. An examination of the various quality factors (Table 3.2) shows large differences between the two groups, where the meandered resonators (6 GHz) support a higher quality factor. This difference can be explained by the fact that all our energy loss calculations were performed for a straight line geometry. For example, the radiation loss of a meandered resonator could be larger than that of the straight line resonator. In addition there are other losses that might occur at the curves.

As stated above, Q depends on the input power, the larger the input power the larger

f_0(GHz)	Q
4.3458	302900
4.5346	41673
4.7572	40202
6.1129	659850
6.1995	550068
6.3960	80799

Table 3.2: Measured Q and f_0 in high input power, for f_0 lower than 8 GHz. All resonators have the same nominal coupling capacitor.

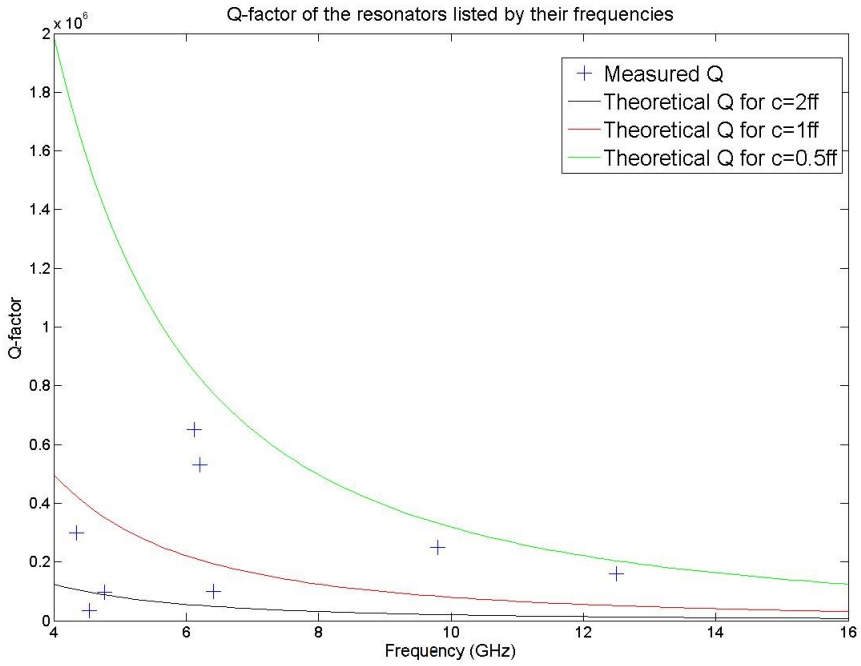

Figure 3.6: The measured Q-factor of the resonators listed by their frequencies (crosses). The other lines shows the theoretical Q-factor for different coupling capacitor when the red marks for C=1ff, the green marks for C=0.5ff and the black marks for C=2ff.

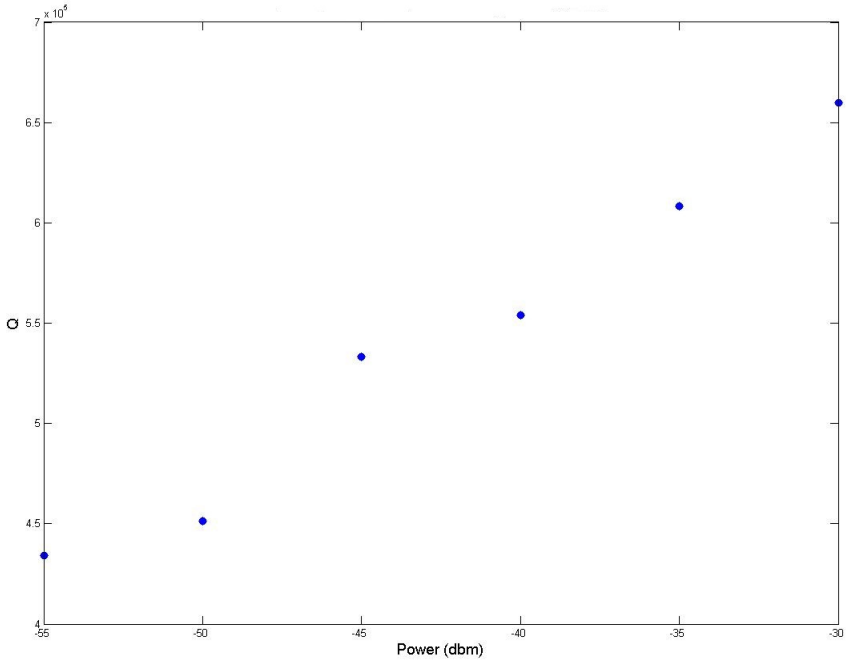

Figure 3.7: This graph shows the dependence of the Q in the input power, for the resonator with $f_0 = 6.11GHz$

the Q, The influence of the input power on the q-factor as shown in graph 3.7 matches the theory described above. However, we can not extract the intrinsic quality factor from this graph without additional points at low power.

Our work focuses in the regime of singles photons, therefore we are interested in the number of photons stored at the resonator at resonance. Using equations 3.9, 3.10 we calculated the number of photons that occupy the resonator at resonance. Figure 3.8 shows the calculated value of the number of photons, as a function of the input power. The main donor to the uncertainty in these values is the power in the resonator off resonance. After taking into account this uncertainty we maintain the same order of magnitude. The linear behavior that is shown in the graph is comprehensible, since the main parameter that has been changed in equation 3.10 is P_{res} while the other parameters have not been significantly changed. Moreover, we can assume from this graph that if we would further decrease the power we might reach the one photon regime. Better amplification will probably allow us to get to the single photon limit.

These high Q resonators will be able to function as readout for a future qubits, furthermore they will allow fabrication of computing devices based on resonators such as the device that

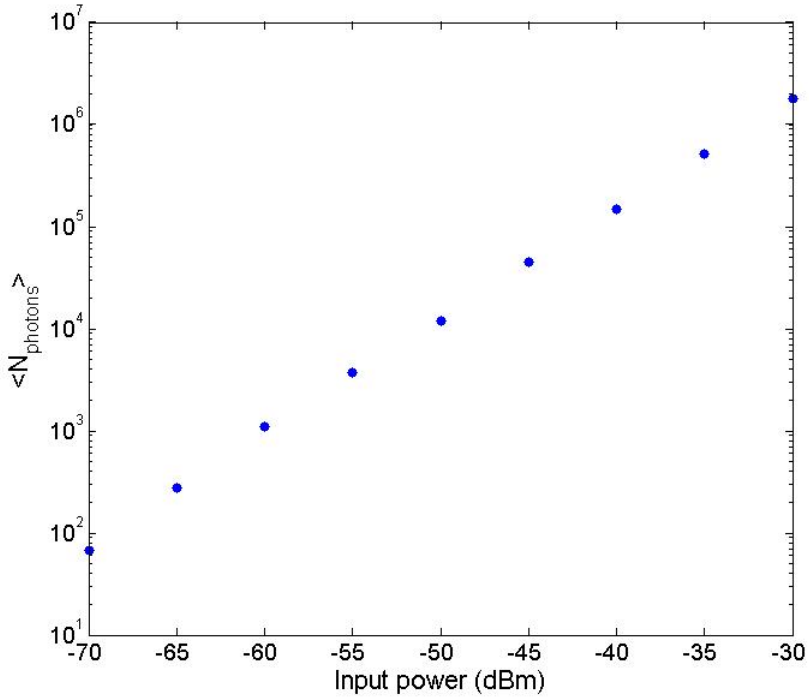

Figure 3.8: Measured number of photons in resonance for different input power (for $f_0 = 6.11GHz$)

will be presented in chapter 5.

Chapter 4

Superconducting Qubit Device

4.1 Introduction

One of the great advantages of a superconducting qubit device as a macroscopic object is the possibility of coupling to other circuits. This benefit comes hand in hand with undesired coupling to the environment. This coupling causes large sensitivity to external noise. These noises have a large effect on the information losses in the state, which results in a reduced coherence time .

4.1.1 Decoherence mechanisms in the Phase qubit

Quantum interaction between the system and the environment leads to non-classical correlations between the state of the system and the degrees of freedom in the environment (entanglement). As a result, the system is no longer described by a pure state having a density matrix $\rho = |\varphi\rangle\langle\varphi|$ but rather by a mixed-state having a density matrix $\rho(t) = \sum_i p_i(t)\,|\psi_i\rangle\langle\psi_i|$ [18]. There are several mechanisms that lead to decoherence, the common one is a relaxation process. Even in the absence of relaxation process, the off-diagonal terms in the density matrix (accounting for the coherence) can decay in time. In a phase qubit there is dephasing that comes from low-frequency fluctuations. The energy levels in the circuit are set by several parameters (depending on the type of circuit), such as the flux bias. When those parameters fluctuate, a random phase is accumulated $\phi(t) = \int^t \omega(t')dt'$, and thus causes the state to dephase relative to the control pulses which (ideally) retain phase correlation between themselves. It should be emphasized that this kind of dephasing is classical, since it results from noise in a classical parameter of the

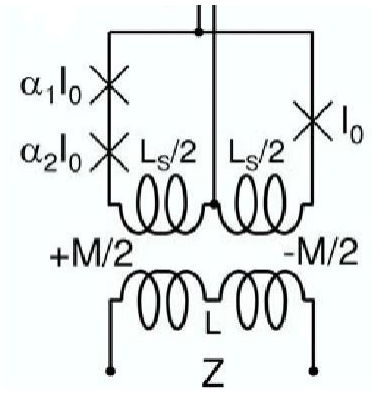

Figure 4.1: A diagram of three junctions squid

system.

4.1.2 Three junctions SQUID - brief introduction

The geometric design and the ratio between the single junction and the pair stand in the base of three junction's squid design as it appears in Neeley's paper [19]. The geometric model is designed in such a way (a symmetrical design) that it will be insensitive to external flux. In addition the sensitivity of three junctions squid (Figure 4.1) to external flux depends on the inductance of the junctions. The junctions are defined by their critical current (I_0), α_2 and α_1. We will design the circuit so that α_2 and α_1 will be equal or close to 2 (practically we designed it to 1.7). In this case when the circuit current is far from the critical current regime (when the Josephson junction behave as a linear inductance) the effective inductance from both sides are the same, and therefore the total mutual inductance is zero. However when the circuit current is close to the critical current (I_0) the non-linearity of the inductance causes the total mutual inductance to be non-zero. This enables measurement of external flux changes.

4.1.3 Noise Analysis

As stated in the general introduction noises have large influence on the coherence time of the qubit. According to **(author?)** [20] we can define an expression of the mean-squared phase due to flux bias noise:

$$\left\langle \phi^2(t) \right\rangle \backsimeq \left(\frac{\partial \omega_{10}}{\partial I_{bias}} \right)^2 S_1^*(1\,Hz) \cdot ln(0.401/f_m t) \cdot t^2 \tag{4.1}$$

where f_m corresponds to the frequency of the entire measurement, and S relates to the power spectrum of the noise, based on experiments. When an explicit expression for the coherence time (T_2), obtained from finding the minimal time that solves the inequality $\langle \phi^2(t) \rangle \geq 2\pi$ (when the variance of ϕ is more than 2π the uncertainty in ϕ is maximum). The expression for the resonance frequency in phase qubit is:

$$\omega_{10} \backsimeq \omega_p \left(1 - \frac{5}{36} \cdot \frac{\hbar\omega_p}{\Delta U}\right) \qquad \omega_{21} \backsimeq \omega_p \left(1 - \frac{5}{18} \cdot \frac{\hbar\omega_p}{\Delta U}\right) \tag{4.2}$$

where

$$\omega_p(I) = \left(\frac{2^{\frac{3}{2}}\pi I_0}{\Phi_0 C}\right)^{\frac{1}{2}} \left[1 - \left(\frac{I_{bias}}{I_0}\right)^2\right]^{\frac{1}{4}} \qquad \Delta U(I) = \left(\frac{2^{\frac{3}{2}} I_0 \Phi_0}{3\pi}\right) \left[1 - \frac{I_{bias}}{I_0}\right]^{\frac{3}{2}} \tag{4.3}$$

and the mapping of current bias to flux bias is[21]:

$$I_0 = I_0^{'} sin(\delta_0) \qquad I_{bias} = \left(\Phi - \frac{\delta_0 \Phi_0}{2\pi}\right) \cdot \frac{1}{L} \tag{4.4}$$

According to these relations we ran a simulation that checked the influence of increasing the circuit's inductance on the coherence time, while we kept the resonance frequency around 6 GHz by tuning the capacitance and the critical current. The values that we used for S_I and f_m were $S_I = (10^{-6} * \Phi_0)^2 / L^2 \qquad S_I^* = S_I \cdot f_m$ and $f_m = 10^4 Hz$. The most important thing that came out from the simulation was the prediction that increasing the inductance would lead to a linear increase in the coherence time (Fig 4.2).

4.1.4 The effect of a chain of junctions

The inductance in the superconducting qubit can be classified into two classes, the geometric inductance and the Josephson inductance. The geometric inductance refers to the inductance that is due to the geometric pattern of the circuit (like classical inductance). The Josephson inductance refers to the inductance due to the nonlinear behave of Josephson junction. Based on this classification we can classify and examine the possibilities of increasing the inductance. The first possibility is to increase the geometric inductance by increasing the area of the loop. The disadvantage inherent in this method lies in the fact that it increases the mutual inductance which leads to the strengthening of the coupling to the environment, action that increases the influence of noises. The second possibility is based on the behavior of the Josephson junction. Josephson junction can be compared to

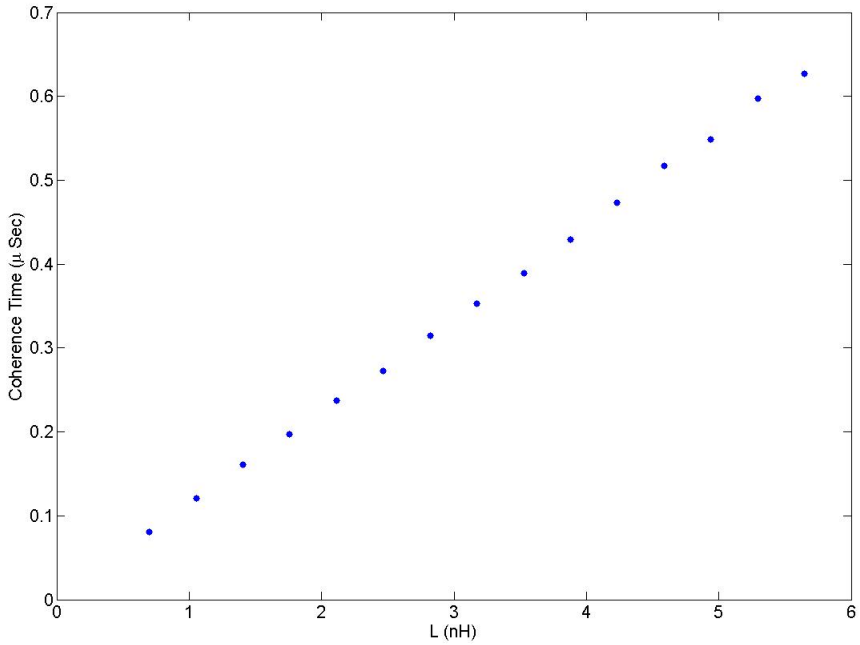

Figure 4.2: T_2 as a function of the inductance (L).

a nonlinear inductor ,where the expression of this inductance is:

$$L_j = \frac{\Phi_0}{2\pi \left(I_0^2 - I^2\right)^{\frac{1}{2}}} \qquad L_{j-linear} = \frac{\Phi_0}{2\pi I_0} \tag{4.5}$$

Based on these equations, we assume that adding junction to the circuit will increase the inductance. There are several problems that can arise during the implementation of this assumption. When a new Josephson junction is added to the circuit it can change the nonlinear element in the Hamiltonian (clearly not desired). We can avoid this problem by working in a regime of $I \lll I_0$ when the 'inductance' is linear (Eq 4.5) and effectively the Hamiltonian will look the same as the Hamiltonian of a single junction circuit.

Implementation of this assumption does not involve any increase in the geometric inductance, moreover, it allows us to decrease the geometric inductance (geometric inductance (mutual inductance) is necessary in order to couple the qubit to the squid and the flux bias).

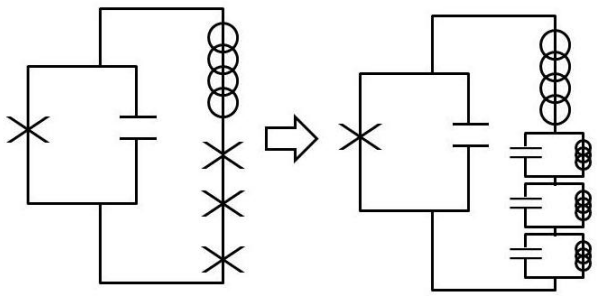

Figure 4.3: An equivalent circuit as a lumped elements circuit

4.1.5 Decay (Losses)

There is a great importance to processes that cause energy losses, which define the lifetime of the qubit. In addition to the usual elements that cause losses, in our design we added a unique element, a chain of junctions. By definition any junction has a capacitance. This capacitance is very small in comparison to the large capacitance in the circuit, so it does not influence the total capacitance of the qubit. However, any small capacitor has a loss tangent (an imaginary component at the capacitance value) which translats to losses. In order to verify that the decay time of the qubit does not decrease when we insert the chain we checked the Q factor of our qubit's equivalent circuit (Figure 4.3). We ran a simulation that calculated the impedance of the circuit for several different values of loss tangent. We set the following parameters $C = 0.6\,pF$, $L_{geometry} = 0.2\,nH$, $I_0 = 0.5\,\mu A$ and 30 junctions at the chain. For $tan(\delta) < 10^{-4}$ we get a Q factor higher than 10^5 and by using $T_1 = \frac{Q}{2\pi\omega_0}$ we get $T_1 > 1\mu S$ (figure 4.4). Since typical T_1 is around $100\,nSec$, we can neglect the energy loss of the chain.

4.2 Mask Design

The complete design includes three main parts: squid, flux bias and qubit. Beside of these three parts there are also pads, alignment marks, test structures, etc. In this section I will review the considerations and calculations that guided us in selection and calculation the parameters. All the inductance calculation has been done by using Fast Henry and Fast Model. The mask was drawn using L-Edit.

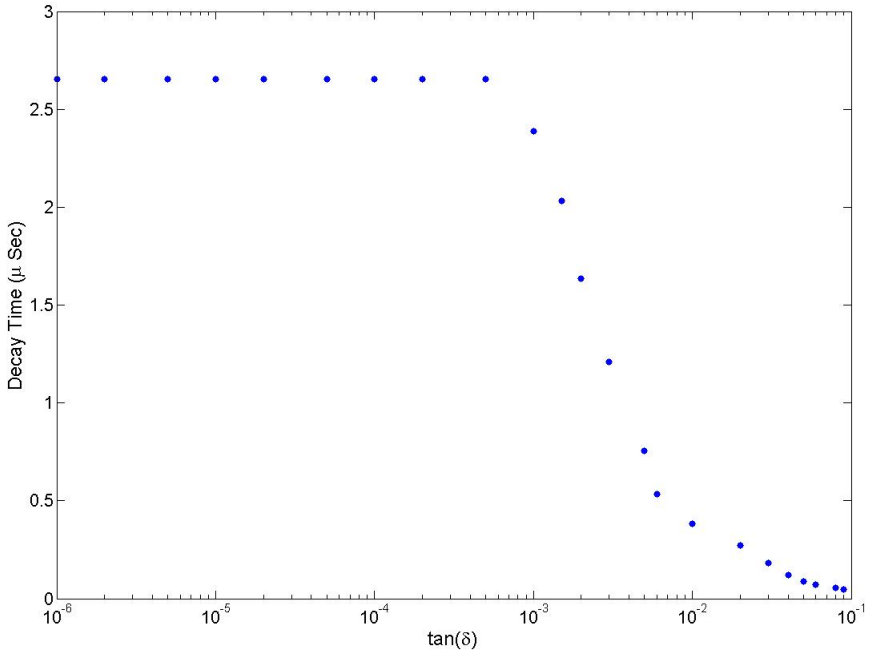

Figure 4.4: Dependance of T_1 on the loss tangent ($tan(\delta)$) of the added Josephson junctions, for a circuit contains 30 junctions

4.3 Result & Discussion

The qubit is currently in the production process, we hope to characterize it in the near future.

Chapter 5

Quantum Random Walk

5.1 Introduction

In August 1993 Aharonov Davidovich and Zaguri published a paper [22] that introduced the concept of quantum random walk (QRW). They showed (theoretically) that due to quantum interference effects the average path length can be much larger than the maximum allowed path in the corresponding classical random walk. As we know in classic RW when the probability of going left or right is the same (on the integer number line (Z)), the standard deviation is $\sigma = \sqrt{N_{steps}}$ where N_{steps} is the number of steps. In QRW we get different results due to the quantum interference effects. Since that paper was published several works which show QRW effect have been done via a quantum optic system. In order to see the phenomenon of QRW in a superconducting quantum device, we describe a superconducting application and simulation that shows that QRW phenomenon could be seen in this application.

Many research groups in computer science are expressing interest in QRW. They are searching for a new quantum algorithm that uses QRW. Due to it we can look on QRW as another tool in our quantum computer "toolbox".

5.2 Theoretical experiment

5.2.1 Experimental Design

The system which we intend to investigate, in order to see QRW, is a chain of superconducting resonators (Figure 5.1) , that are coupled in a row (for readout we can use a

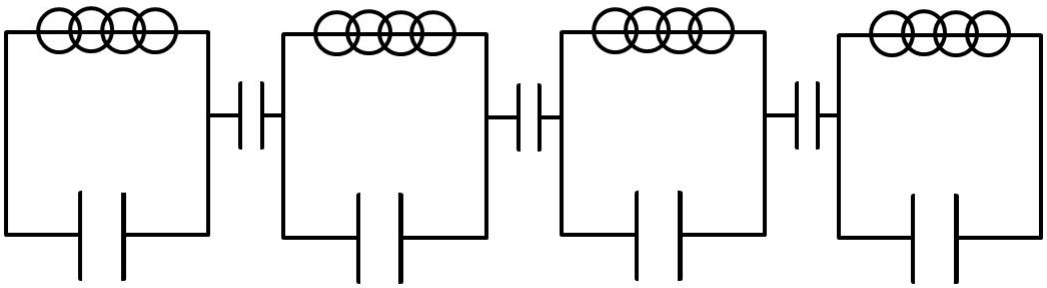

Figure 5.1: A diagram of four coupled resonators an example of the system we intend to investigate. Any resonator should be coupled to a readout device (not appeared in the figure)

qubit). Each resonator simulates coordinate in a dimension that contains N points (N is the number of the resonators). By driving individual particles in the resonator with a microwave source and detecting the output field of the resonators at different times, we can investigate the dynamic of the particles in our "resonator space". Our "new world" has two main parameters. The first one is the number of resonators (N) which determines the space. The second parameter is the coupling capacitor between neighboring resonators. In a setup with one particle and two resonators the particle will "jump" from one resonator to the other with a frequency of Ω, where Ω is related to the coupling capacitance.
In case of more than one particle the frequency depends on the number of particles as: [23]

$$\Omega_n = \Omega_0 \cdot \sqrt{n} \tag{5.1}$$

where n is the number of particles, Ω_0 is the frequency in the case of one particle and Ω_n is the frequency in the case of n particles.
The Hamiltonian that represents this setup is:

$$H = \frac{\Omega_0}{2} \sum_{i=1}^{n-1} (a_i^+ a_{i+1} + a_i a_{i+1}^+) \tag{5.2}$$

5.2.2 Simulation

In the usual case if we want to span our vector space we need a basis that contains n^N vectors (n is the initial number of particles and N is the number of resonators). In our case we use the fact that the sum of the particles in the system is less or equal to n (due to lsses)

and represent the state by a reduced basis. For example in the case of $n = 2,\ N = 2$ the full basis includes (0,0), (0,1), (1,0), (1,1), (2,0), (0,2), (2,1), (1,2), (2,2) and the reduced basis includes (0,0), (0,1), (1,0), (1,1), (2.0), (0,2). This method enables us to work faster and with larger values of n and N. The disadvantage of this method is that it is very complicated, therefore the simulation has been written for one or two particles. The core of the simulations is the evolution in time of the states. The time evolution operator consists of two parts, the Hamiltonian that was presented in the previous paragraph and the decay operator.

5.2.2.1 Decay

The main theory behind the building of the decay operator has been taken from the case of a single resonator in Nielsen & Chuang book [18]. Based on the assumption that resonator interacts with an environment can be modeled as another harmonic oscillator, the decay Hamiltonian is:

$$H_d = \chi(a^+ b + a b^+) \tag{5.3}$$

where b is the annihilation operator of the environment and χ equal to square root of one over the decay time. In the case of a single resonator and n photons the decay elements (E_k) are:

$$E_k = \sum_n \sqrt{\binom{n}{k}(1-\gamma)^{n-k}\gamma^k}|n-k><n| \tag{5.4}$$

where

$$\gamma = 1 - cos^2(\chi\sqrt{\Delta t}) \tag{5.5}$$

and the decay operator ε_d is:

$$\varepsilon_d(\rho) = E_0 \rho E_0^+ + E_1 \rho E_1^+ + ... \tag{5.6}$$

It is important to note that the element E_k connects to the k-th order of the decay operator. In our case we have N resonators so we use Kronecker product between N elements. The zero order of the decay elements is $E_0^{\times N}$ ($E_0^{\times N}$ means $E_0 \times E_0 \times E_0 \times E_0 \times ...$ N times), the first order is $E_1 \times E_0^{\times N-1} + E_0 \times E_1 \times E_0^{\times N-2} + E_0^{\times 2} \times E_1 \times E_0^{\times N-3} + ...$ and go on for higher order. In our case we approximated the decay operator until the first order only.

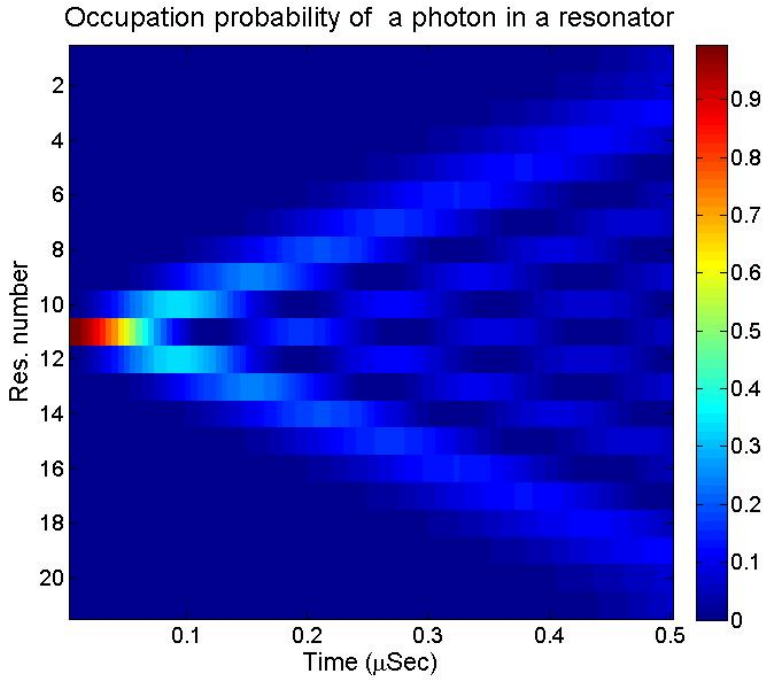

Figure 5.2: The propagation of a single photon without a decay effect. The system contains 21 resonators with coupling frequency $\Omega = 10$ MHz

example: In the case of one resonator and one photon the elements E_k will be:

$$E_0 = \begin{bmatrix} 1 & 0 \\ 0 & \sqrt{1-\gamma} \end{bmatrix} \qquad E_1 = \begin{bmatrix} 0 & \gamma \\ 0 & 0 \end{bmatrix} \tag{5.7}$$

5.2.2.2 Simulation result

We ran the simulation on a single and double particles. The propagation of one particle is shown in Figure 5.2. It can be seen that unlike classical random walk the probability after some time does not look as a normal distribution (Gaussian) as it looks in classical RW . Figure 5.3 shows the propagation of an initial state containing two photons in the fourth resonator . In order to get an approximation of the number of resonators that are required for the removal of edge effects (as seen in Figure 5.3 by the bouncing of two particles from the edges) we ran the simulation in the case of a single photon with decay (the other parameters were the same as the case with a decay). Figure 5.4 shows that less than 30 resonators can be satisfying, in order to get maximum information on the diffusion of a single photon (in this specific case).

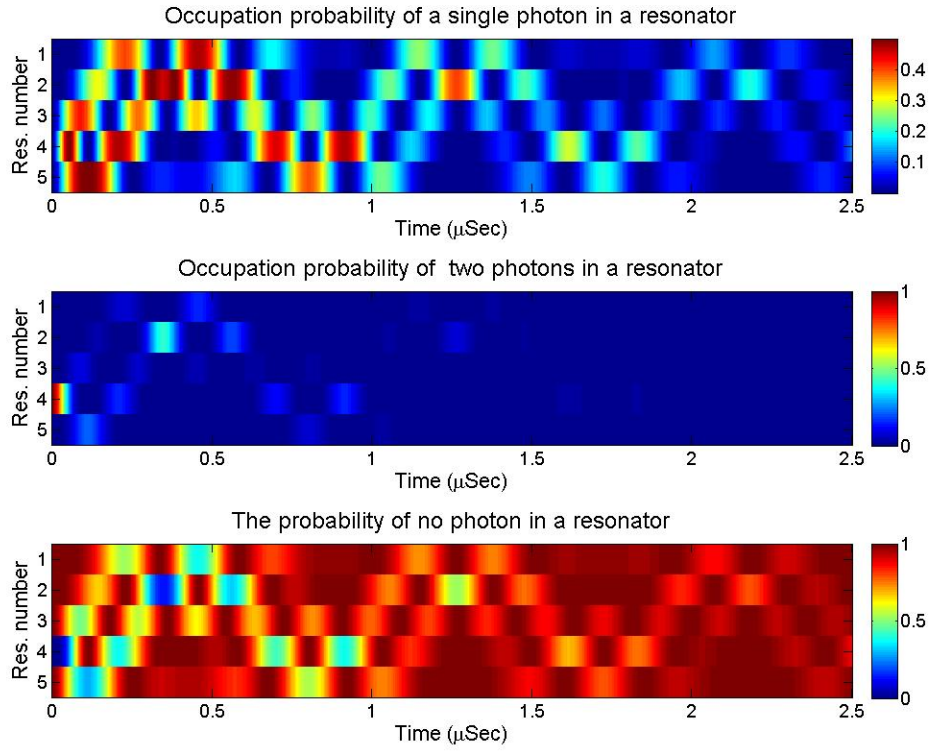

Figure 5.3: The propagation of two photons. The system contains five resonators with coupling frequency $\Omega = 10MHz$ and $T_1 = 2.5\mu Sec$. The initial state is two photons in the third resonator.

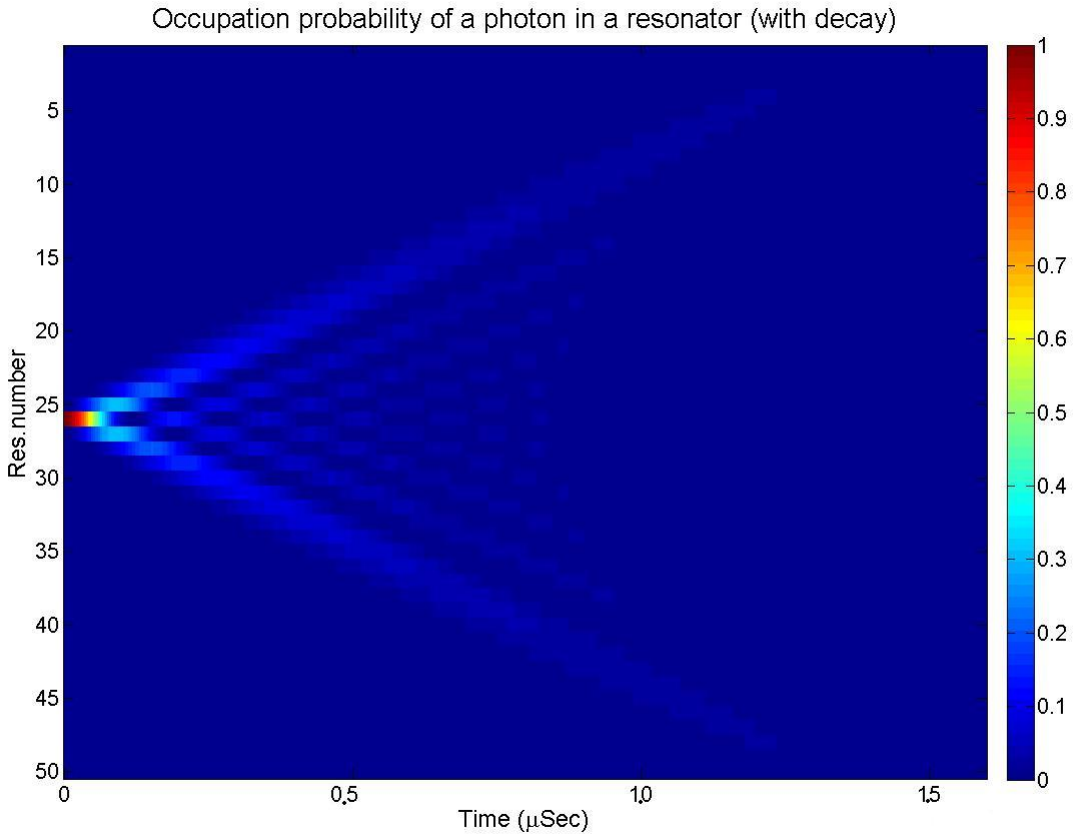

Figure 5.4: The propagation of a single photon with a decay effect. The system contains 50 resonators with coupling frequency $\Omega = 10\text{MHz}$

5.3 Discussion

As the simulation shows we can see the QRW effects in a system of coupled resonators. In addition, for specific parameters we can find the number of resonator that are required for the removal of edge effects. However, we need to take into further consideration the required frequency ,Ω, for the specific decay time of our system. The simulation has not been tested for more than two particles. The simulation can also be extended to larger spaces.

Chapter 6

Summary

Based on the inductive behavior of Josephson junctions, which can be used to increase the inductance of a circuit, we have presented in this thesis a new design of the phase qubit. We show by simulation an improvement in the coherence time of the new design in comparison to the traditional phase qubit. This new design will be fabricated and characterized in the near future. Short coherence time is one of the major problems that inhibit the continued use of qubits for research and implementation of various algorithms. Long coherence times allow coupling larger number of qubits which is necessary for the advancement of quantum computation. In addition it will enable taking measurements that today are found to be difficult to perform due to the time limit, e.g weak measurements, multi-level system measurements etc.

We also show microwave superconducting resonators which support a high quality factor (more than 100,000), at the low power limit of only a few tens of photons. Such resonators can function as readout devices for a qubits or as a part of a research setup, functioning as harmonic oscillators. In the last part of the thesis we described a setup that examines the Quantum Random Walk (QRW) phenomenon, using an array of a coupling resonators. In the simulation . Extending the simulation to more than two photons and an implementation of this setup, can be used for some QRW based quantum algorithms .

Another important ability that was acquired, as a result of our resonators measurement, is the ability to characterise dielectric material using superconducting resonators. Fabricating the resonators on a dielectric material and measuring the Q factor will give information on the loss tangent of the material.

Bibliography

[1] Michael Tinkham. *Introduction to Superconductivity: Second Edition (Dover Books on Physics)*. Dover Publications, June 2004.

[2] Michel H. Devoret. "quantum fluctuations in electrical circuits". 1995.

[3] G. Wendin and V.S. Shumeiko. "superconducting quantum circuits, qubits and computing". 2008.

[4] A. Wallraff M.H devoret and J. M. Martinis. "superconducting qubits: A short review". 2008.

[5] Michel H. Devoret and John M. Martinis. Implementing qubits with superconducting integrated circuits. *Quantum Information Processing*, 3(1-5):163–203, 2004.

[6] Jens Koch, Terri M. Yu, Jay Gambetta, A. A. Houck, D. I. Schuster, J. Majer, Alexandre Blais, M. H. Devoret, S. M. Girvin, and R. J. Schoelkopf. Charge-insensitive qubit design derived from the cooper pair box. *Physical Review A (Atomic, Molecular, and Optical Physics)*, 76(4):042319, 2007.

[7] Jay M. Gambetta B. L. T. Plourde Jerry M. Chow A. D. Corcoles John A.Smolin Seth T. Merkel J. R. Rozen George A. Keefe Mary B. Rothwell Mark B. Ketchen Chad Rigetti, Stefano Poletto and M. Steen. 'superconducting qubit in waveguide cavity with coherence time approaching 0.1ms'. 2012.

[8] Leonid I. Glazman Michel H. Devoret Vladimir E. Manucharyan, Jens Koch. Fluxonium: Single cooper-pair circuit free of charge offsets'. 2009.

[9] Dmitri G.Starodoub. *Role of atomic transport in evolution of nano scale oxide structures*. PhD thesis, 2009.

[10] Markus Ansmann. *Superconducting Josephson Phase Qubit: The Violation of Bell's Inequality*. PhD thesis, 2003.

[11] Benjamin A. Mazin. *MicroWave Kinetic Inductance Detectors*. PhD thesis, 2004.

[12] A. Vayonakis and J. Zmuidzinas. "radiative losses from 2d apertures". 2001.

[13] R. C. Bialczak M. Hofheinz N. Katz Erik Lucero C. McKenney M. Neeley H. Wang E. M. Weig A. N. Cleland Aaron D. OConnell, M. Ansmann and J. M. Martinis. "microwave dielectric loss at single photon energies and millikelvin temperatures". 2008.

[14] Benjamin A. Mazin Anastasios Vayonakis Jonas Zmuidzinas Peter K. Day, Henry G. LeDuc. A broadband superconducting detector suitable for use in large arrays. 2003.

[15] Aaron D. O'Connell, M. Ansmann, R. C. Bialczak, M. Hofheinz, N. Katz, Erik Lucero, C. McKenney, M. Neeley, H. Wang, E. M. Weig, A. N. Cleland, and J. M. Martinis. Microwave dielectric loss at single photon energies and millikelvin temperatures. *Applied Physics Letters*, 92(11):112903, 2008.

[16] H. Wang, M. Hofheinz, J. Wenner, M. Ansmann, R. C. Bialczak, M. Lenander, Erik Lucero, M. Neeley, A. D. O'Connell, D. Sank, M. Weides, A. N. Cleland, and John M. Martinis. Improving the coherence time of superconducting coplanar resonators. *Applied Physics Letters*, 95(23):233508, 2009.

[17] David M Pozar. *Microwave Engineering, third edition.* 2005.

[18] Michael A. Nielsen and Isaac L. Chuang. Quantum computation and quantum information. October 2000.

[19] Radoslaw C. Bialczak M. Hofheinz N. Katz Erik Lucero A. OConnell H. Wang A. N. Cleland Matthew Neeley, M. Ansmann and John M. Martinis. 'transformed dissipation in superconducting quantum circuits'. 2008.

[20] John M. Martinis, S. Nam, J. Aumentado, K. M. Lang, and C. Urbina. Decoherence of a superconducting qubit due to bias noise. *Phys. Rev. B*, 67(9):094510, Mar 2003.

[21] John M. Martinis. Mapping of flux-bias to current bias circuits in a phase qubit, 2006.

[22] L. Davidovich Y. Aharonov and A.Zaguri. "quantum random walk". 1993.

[23] R. Bialczak E.Lucero M. Neeley A. OConnell H. Wang J.M. Maritinis M. Hofheinz, E.M. Weig M. Ansmann and A.N. Cleland. "generation of fock states in a superconducting quantum circuit". 2008.

[24] T. L. Robertson, B. L. T. Plourde, T. Hime, S. Linzen, P. A. Reichardt, F. K. Wilhelm, and John Clarke. Superconducting quantum interference device with frequency-dependent damping: Readout of flux qubits. *Phys. Rev. B*, 72:024513, Jul 2005.

Appendix 1

Mask design

As mention above the geometry of the junction is quite straightforward and does not require many parameters. This appendix will discuss on the goal and the designed of each layer/mask (there are three masks).

Base Layer

This layer contains two pads connected by a $50\mu m$ wide wire.

Junction Layer

Similarly to the base layer, the junction layer also contains pads and a wire, but in addition has an aluminum triangle which overlaps with the wire from the base layer creating the junction (Figure 2.1 at right). This layer also contains a thick wire ($50\mu m$) that overlaps with the base layer to create a shunt. The function of the shunt is discussed in the next section.

Third Layer (Removing the Shunt)

This paragraph is a bit misleading, because it does not actually discuss a third layer, but rather the need for a third mask or more specifically, a third lithography step. During the dry etch there is a plasma (detailed below), which creates an electric field. Just as a capacitor could be destroyed under high gradient of voltage, Josephson junction could also be destroyed, depending on the type of material and the thickness of the isolated layer. In order to avoid destruction of the junction during the etching, we design a shunts in the second layer (a 50×50 μm^2 overlapping area) as written above. This shunts eliminates charge differences on the junctions during the fabrication of the junction layer but must be

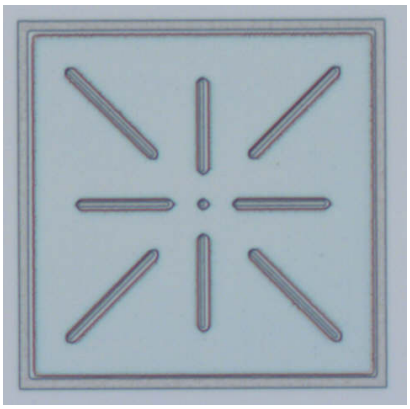

Figure 1: The alignment mark between two layers, in this case it can be seen a mismatch of about one micron.

removed afterwards. The third layer contain eighteen 'windows' which are used to remove the shunts. Obviously we can not use dry etch for that, therefore this step is done by wet etching (Fig 2.1).

Alignment marks

One of the most important and sensitive parts in the fabrication process is the alignment between the layers. To align the layers we used two kinds of alignment marks. The first is a cross-shape , in the other layer there is an inverse mark (Fig 1) . The second alignment mark is a matrix of $4 \times 4\mu m^2$ squares with spacing of $4\mu m$, The corresponding alignment mark in the second layer is a matrix of $2 \times 2\mu m^2$ with different spacing. The second alignment mark has done to get information about the mismatch between the layers.

Appendix 2 -Qubit Design Consideration

Flux bias

As mentioned in the chapter that disscus on the qubit, the main goal of the qubit design is to reduce the geometric inductance and increase the total inductance. Reducing the geometric inductance of the qubit has a direct influence on the coupling with the flux bias, which require us to increase the flowing current in the "flux loop" in order to get the same influence. The maximum current that can be used in our system is around 0.3 mA. According to the equation $\Phi = I_q L_q + M_{fq} I_f$ if we want to save the value of $M_{fq} I_f$ when M_{fq} reduces we need to increase I_f by the same factor. In our specific case the mutual inductance decreases by half so we will double the current. Usually we need I_f to be around $0.1mA$ at the maximum, in order to get a full scan of branch of the squid steps, where $I_0 = 1.5\,\mu A$ and $L \sim 1nH$. In our case $I_0 = 0.5\,\mu A$ and $L \sim 3 - 5nH$ so we need almost the same current. Calculating the width of the branch is done by using the equation

$$\delta_0 = \frac{\Phi_0}{2\pi L I_0} \qquad \frac{\sqrt{1-\delta_0^2}}{\delta_0} - arccos\,(-\delta_0) = l\pi \tag{1}$$

, where l is the total branch width which determine the regime of the current that we need to scan. .

Since high current flow in the flux line we designed this line to be thicker - 5 microns.

Flux parameters that designed: Flux long side length=9μm, Flux short side length=3 μm and this corresponding to a mutual inductnce of $M_{fq} = 0.0017\,nH$.

Squid

The squid's small junction is three time larger than the qubit main junction in order to increase the signal to noise ratio, while keeping the plasma frequency of the squid well above the qubit frequency.

Squid parameters that designed::$SquidSideLength = 40\,\mu m, QbitSideLength = 35\,\mu m L_s = 0.3\,nH$, $L_q = 0.2\,nH M_{sq} = 0.04\,nH$ (the gap between the qubit and the Squid is small as could (1µm).

Qubit

This is the heart of our circuit, it contains four elements: capacitor ,inductor ,main junction and chain of junctions. This paragraph will explained the considerations and goals that were taken for any elements of the qubit. The specific values of any component (critical current, capacitance etc.) were calculated based on simulation.

The simulation

We ran a simulation, in Matlab, in order to get an estimate values for the inductance, the capacitance and the critical current. The simulation calculated the energy levels of the phase qubit (using the phase qubit Hamiltonian 1.3) for a matrix (3D) that contains a different values of L, C and I_0. The simulation's goal was to check that the qubit has a large non-linearity regime and that the qubit has the required resonance frequency.

The capacitor

The goal of the capacitor is to set the resonance frequency to the desired value. Without the capacitor the circuit has capacitance of $\sim 50ff$. This capacitance with inductance of $1nH$ gives a resonance frequency of about $30GHz$. That means too much energy which can cause the aluminum to get out of the superconducting mode. In the design we choose to use two interdigitated capacitors that are connected in parallel. In case that the gap between two digits equal to the digit width (in our design both of them equal to one micron) the capacitance ,in femto farad, of interdigitated capacitor can be calculated by $C = 0.1 \cdot l \cdot N$ [24**?**]where N is the number of digites and l is the length in microns. In our design $l = 125\ \mu m$ $N = 24$ so we get $C = 0.6pF$

The inductor

The inductance of the qubit is composed of two parts: one is the geometric inductance and the second is the chain. The geometric inductance is the same in all designs and it was designed using Fast-Henry so the inductance is around 0.2 nH. Following the fact that we want the qubit to be insensitive to external magnetic fields, the inductance design contains two identical squares that connect in such way that the current that flow in the loop creates a magnetic field in opposite directions.

The main Junction

The main junction was designed for critical current of $0.5\,\mu A$ by seting its area to $1\mu m^2$ (there is one design with area of $2\mu m^2$).We put the main junction above the capacitor because we want to look at the capacitor's center as fat electrode (Fig) so the main junction, the capacitor and the chain contacted in parallel. Another reason for this placement is to keep the junction as far as possible from the geometric inductor.

Array of junctions

According to equation 4.5, if we want to be able to assume that the junction is functioning as an inductor we need to be at the regime $I \lll I_0$. The area of any junction at the chain was chosen to be four times the main junction's area, so we get $4I_{0\,Main\,Junction} = I_{0\,Chain\,Junction}$ and our measurements are carried out near $I_{0\,Main\,Junction}$ .This will put us in the regime that we want.

Other

In the following section I will briefly discuss some little things that were left.

alignment mark - We put a series of a alignment marks such in the junction's design, where there are two "free" series for future use. In addition, we put some more crosses at the edge so we could look on them at the same time (in the Mask aligner machine) and give correction to the angle.

lines/gap width - Flux: the wire thickness is 5 µm and the gap 2.31 µm so we get 50Ω. qubit, Squid – the wire thickness is 2 µm and the gap 0.91 µm.

Test stracture - We put four junctions so we can make a measurement of the critical current of the device at room temparture. The area of the junctions are 1,2,4,8 µm^2 .

Trace width	Gap width
3	1.36
4	1.81
6	2.72
7	3.17

Table 1: A trace width and the corosponding gap width in order to receive 50Ω

Convention about the alignment - In order to avoid from mismatch at the alignment we made a safety area of $1.5\,\mu m$ at each side.

Big junction for ground - When we want to connect the line from the third layer to the ground it becomes a problem (because we would not want to create a junction). In order to solve this problem we made the connection very big, so the new junction functions like a shunt.

Pads - The pads size are $200\mu m \times 200\mu m$m, except squid and flux pads that were modified to get 50Ω(coplanar waveguide theory).

Ground plane - Like in the resonator we made a ground plane with $5\mu m^2$ hole's area.

Resonator – we add a single device that] functions as a resonator. However, this resoantor combined from chain of junctions, capacitor and coupling capacitor (2 ff) (we removed the squid, flux and junction). The resonance frequency of this device should be around 3GHz. The purpose of this resonator is to check the idea of using array of junctions as inductor work.

Appendix 3 - Fabrication 'Recipes'

The purpose of this appendix is to detail the required parameters during lithography and etching processes, as well as placing emphasis on the potential problems at each stage. The appendix will be divided into three parts: lithography, dry etching and wet etching. Excluding lithographs process which we have developed processes for two different methods, other processes were carried out by only one method.

Lithography

As written above the lithography process can be performed by two different methods significantly different from each other. Using 'contact lithography' requires preparation of a chrome mask in a timely manner, while the use of direct writing does not require that on the one hand but takes much longer in the other hand (several hours versus several seconds). In our devices we used both methods. It is important to emphasize that after exposing the photo-resist (PR), there is need for developing. For both methods we used the same PR ,AZ 1505 and the same developer ,AZ developer for Al, when development times were different in each method.

Mask Aligner

Manufacturer and model: Suss MA06. In order to accept accuracy of sub - micron, we blocked some wavelengths by using the filter.

Parameters:

Exposure time - 1.4 sec.

develop time - 30 sec.

Direct Write

Manufacturer and model: Microtech LaserWriter. This instrument has a great advantage by allowing different exposure intensities in different areas. This feature allows us to test once the impact of the different exposure intensities, for a given development time. For finding the parameters we have prepared a design containing lines and squares of different thicknesses, we clone this pattern fifteen times (Fig 2). Using this design allowed us to examine fifteen different exposure intensities at single writing. During the writing, the laser performs a snake-shaped trajectory, when the trajectory width is determined by the lens that used and the movement at the Y-axis is determined by a parameter called D-step. To accept sub-resolution - we want to use micronized lens that gives the smallest beam radius (lens 5).

Parameters:

D-step - 2 (0.2 micron space).

Gain - 1.5 (when the dimmer is on).

develop time - 65 sec.

Potential problems As mention above the laser performed a 'snake shape' trajectory during the writing. As a result of this trajectory, his speed is not completely constant, there is a slowdown before the rounds, meaning that the exposure time naturally is higher there. To avoid this problem there is an automatically correction for the intensity of exposure. One of the problems we dealt with was that for low exposure intensities the automatically correction was not enough, causing the formation of 'unexposed' regions in the edges (Fig 2). The solution of this problem was by changing one of the internal parameter.

Dry Etching

Manufacturer and model: Oxford Instruments Plasmalab System 100. The etching process contains three main steps: punch-through, slow etch ($\sim 100\frac{nm}{min}$) and remove PR, when before any step we run a pumping for 30 seconds.

Parameters:

HBr - 5 sccm , Ar - 75 sccm

ICP power - 600 - 800 W

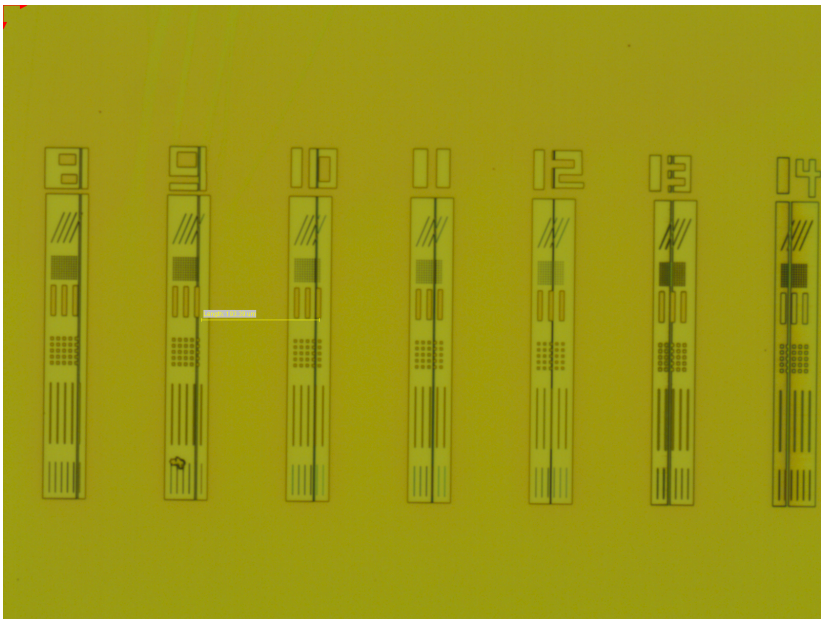

Figure 2: The designed pattern that we used for testing the parameters. The observed lines are the unexposed areas,as it described in the potential problems section, problem that solved by changing internal parameters of the Machine

temperature 60 C

Wet Etching

The acid which was by us for the etching, was a mixture of: H3PO4 (Phosphoric acid), HNO3 (Nitric acid) and Acetic acid

Parameters:

temperature - 40-50 C

time - 5-10 min